Available online at www.sciencedirect.com
ScienceDirect
Ore Geology Reviews 32 (2007) 125–156
ORE GEOLOGY REVIEWS
www.elsevier.com/locate/oregeorev

Geological and geochemical characteristics of the Sawaya'erdun gold deposit, southwestern Chinese Tianshan

Jiajun Liu [a,b,c,*], Minghua Zheng [d], Nigel J. Cook [e], Xunrong Long [d], Jun Deng [a], Yusheng Zhai [a]

[a] *State Key Laboratory of Geological Processes and Mineral Resources, China University of Geosciences, Beijing 100083, People's Republic of China*
[b] *Key Laboratory of Ore Deposit Geochemistry, Institute of Geochemistry, Chinese Academy of Sciences, Guiyang 550002, People's Republic of China*
[c] *State Key Laboratory of Mineral Deposit Research, Nanjing University, Nanjing 210093, People's Republic of China*
[d] *School of Earth Sciences, Chengdu University of Technology, Chengdu, 610059, People's Republic of China*
[e] *Natural History Museum, University of Oslo, Boks 1172 Blindern,0318 Oslo, Norway*

Received 7 October 2004; accepted 12 November 2006
Available online 31 January 2007

Abstract

The Sawaya'erdun gold deposit in the western segment of the South Tianshan, Xinjiang, China, is a large, low-grade orogenic gold deposit. An abundance of index fossils in the ore-hosting strata, including brachiopoda, corals and *Schwagerina*, show that the fossil age of the country rocks ranges from Late Carboniferous to Early Permian. Whole rock Rb–Sr and Sm–Nd isochron ages, ranging from 292.43±0.38 to 304.7±11.6 Ma, are concordant with a Late Carboniferous age. Gold mineralization is strictly controlled by a fault zone. Ore minerals are dominated by sulfides, with gold inhomogeneously distributed within them; gangue minerals are quartz, siderite or calcite. Data suggest that the ore-forming fluid was derived predominantly from an active meteoric groundwater system. Ore-forming temperatures are estimated to have been within the range 110 to 220 °C.

New $^{40}Ar/^{39}Ar$ isotope age determinations of auriferous quartz are in excellent agreement with Rb–Sr ages obtained from fluid inclusions in quartz. They suggest gold mineralization at 206 to 213 Ma (Late Indosinian). Such an age is consistent with the age of formation given for other gold deposits in the region, such as Bulong and Dashankou. Combined with K–Ar geochronological data and observed geological features, it is concluded that the Indosinian metallogentic epoch represents a previously unrecognized, major period of gold metallogeny in the southwestern Chinese Tianshan. In some ways, the Sawaya'erdun gold deposit can be compared with the Muruntau gold deposit in Uzbekistan with respect to geological setting, host lithology, mineralization style, mineral assemblages, geochemical association and metallogenic processes involved. Despite this, the Sawaya'erdun gold deposit possesses a number of characteristics typical of only low-temperature metallogenesis.

Keywords: Sawaya'erdun gold deposit; Geochronology; Southwestern Chinese Tianshan

1. Introduction

Investigation of the formation conditions of super-large deposits of gold ore (those in which gold reserves exceed 1000 t (or 33 Moz), Laznicka, 1983, 1989; Tu,

Abbreviations: Py=pyrite; Po=pyrrhotite; Hm=hematite; Mt=magnetite.

* Corresponding author. State Key Laboratory of Geological Processes and Mineral Resources, China University of Geosciences, Beijing 100083, People's Republic of China.
E-mail address: liujiajun@cugb.edu.cn (J. Liu).

0169-1368/$ - see front matter © 2007 Elsevier B.V. All rights reserved.
doi:10.1016/j.oregeorev.2006.11.003

2000) and development of exploration models for this type of deposit are hot topics in modern ore deposit exploration in China and elsewhere (Tu, 2000; Zhai, 2006). According to statistical data (Liu et al., 1998a), only nine super-large gold mineral camps have been discovered throughout the world. One of these is the Muruntau gold deposit in the Tianshan of Uzbekistan (Shayakobov et al., 1999) The Tianshan is recognized as one of the largest gold provinces on Earth and hosts several world-class gold deposits (Seltmann et al., 2003). Muruntau, itself, is the largest gold resource in Eurasia (175 Moz; Goldfarb et al., 2001; Yakubchuk et al., 2002). Similar, but smaller gold deposits, such as Amantaitau (4 Moz), Daugyztau (5 Moz), Charmitan (>10 Moz), Jilau (>3 Moz), Taror (>3 Moz), Bakyrchik (8 Moz), Vasilkovskoye (13.4 Moz), and Kumtor (18 Moz), are identified in Uzbekistan, Tajikistan, Kazakhstan and Kyrgyzstan (Goldfarb et al., 2001; Rui et al., 2002; Yakubchuk et al., 2002), demonstrating the huge exploration potential for such deposits in the eastern extension of the Tianshan Mountains in Xinjiang Province, China (Liu et al., 1999). It is worth noting, at this point, that Kumtor, another large gold deposit, occurs in the western extension of Haerketau Mountains, only 40 km west of the frontier with Xinjiang. The success of exploration in the Central Asian Republics has provided a great impetus to exploration in the southwestern Chinese Tianshan Mountains, with participation by a number of multinational exploration companies (Liu et al., 1998a).

The discovery of the Sawaya'erdun gold deposit in the early 1990s marked an important breakthrough in prospecting for Muruntau-like orogenic gold deposits in the Chinese portion of the Tianshan (Zheng et al., 1996; Li and Luo, 1997; Zheng et al., 1998; Liu et al., 1998a; Zheng et al., 2001; Liu et al., 2002a). Despite this, the Chinese mineral exploration community continues to ask why orogenic Muruntau-like gold deposits occur so extensively in the southern Tianshan Mountains yet are largely restricted to the neighboring countries of China? Secondly, why has it been difficult to achieve further breakthroughs in prospecting for gold deposits of this type within the national boundaries of China?

2. Geological setting

The southwestern Chinese Tianshan Mountains are a portion of the 'South Tianshan Sb–Hg–Au Metallogenic Subprovince'. This metallogenic subprovince extends E–W for more than 3000 km and is separated into western and eastern parts by the post-mineral Talas-Ferghana strike-slip fault. The western part of the metallogenic subprovince is located within the boundaries of the former Soviet Union, where a large number of orogenic gold deposits and occurrences have been discovered. The eastern segment (east of Osh) extends into Xinjiang, China. Great similarities have been recognized in stratigraphy, petrology and tectonic setting on the two sides of the border (Zheng et al., 1996; Liu et al., 1998a; Ye et al., 1998; Liu et al., 2000a; Zheng et al., 2001).

In China, the Tianshan Tectonic Zone can be divided into three belts, i.e., North, Middle and South Belts, corresponding to the Junggar, North and South Tianshan Belts on the Central Asian side of the border, respectively (Liu et al., 1998a). Regional tectonic lines, such as the Nikolaev fault zone, and ore-hosting strata, which both control the location of gold deposits, extend eastwards into the Chinese Tianshan Mountains (Zheng et al., 1996; Liu et al., 1998a; Zheng et al., 2001).

The Sawaya'erdun gold deposit, the largest recognized orogenic gold deposit in Xinjiang Province, with >3 Moz Au proven reserves, and a geologically-inferred resource of at least 10 Moz Au (Rui et al., 2002), was discovered by the No.2 Geological Party of Xinjiang Bureau of Geology and Mineral Resources. The deposit is located in the western part of Late Paleozoic continental marginal basin of South Tianshan. The northern part of the deposit continues eastwards to Kyrgyzstan (Fig. 1). The area around the mine is dominated by strata of the slightly metamorphosed Upper Carboniferous clastic flyschoid formation (Zheng et al., 1996; Liu et al., 1999; Zheng et al., 2001). Carbonate strata, probably of Middle Devonian age, occur in the southeastern part of the mining district. There is a large, NW-dipping reverse fault between the clastic and carbonate rocks (Fig. 2A).

The ore-hosting clastic rocks can be divided into lower, middle and upper lithological segments (Fig. 3). The lower segment is dominated by gray, medium- to thin-bedded, fine-grained quartz sandstone and siltstone intercalated with carbonaceous slate. There is thin-bedded marl and bioclastic limestone at the base (Fig. 2B). The middle segment is the most important ore-hosting part of the succession and is composed of rhythmically interbedded dark gray to black, thin-bedded siltstone and carbonaceous slate. The upper segment is composed predominantly of gray to dark gray, medium- to thin-bedded silty slate, siltstone, pebbled siltstone (Fig. 2C), and carbonaceous slate with a distinct trend of increasing slate/siltstone ratio upwards. At the base of the segment is the typical Bouma sequence (Zheng et al., 1996, 2001).

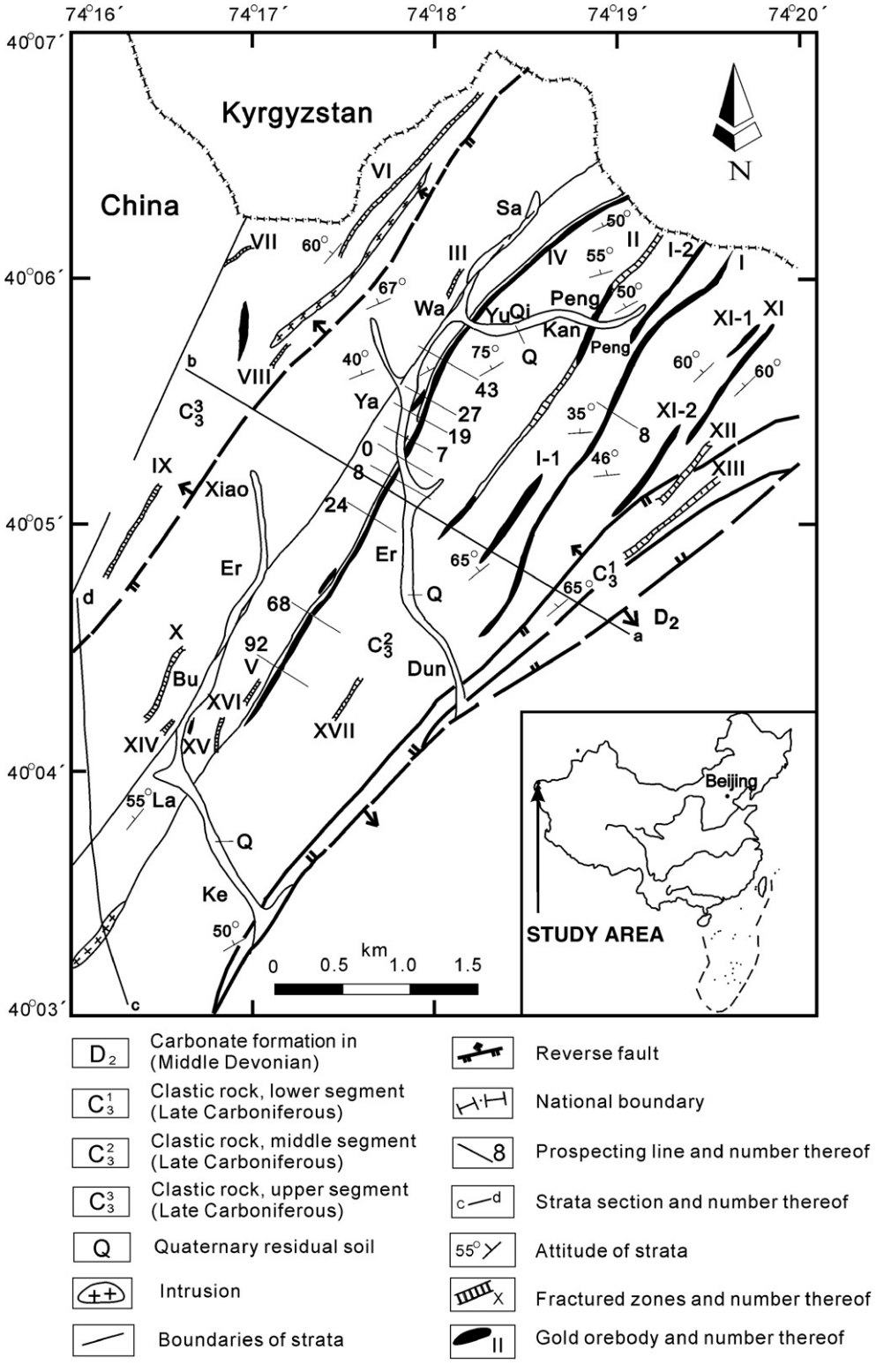

Fig. 1. Geological sketch map of the Sawaya'erdun gold deposit (modified after Zheng et al., 1996).

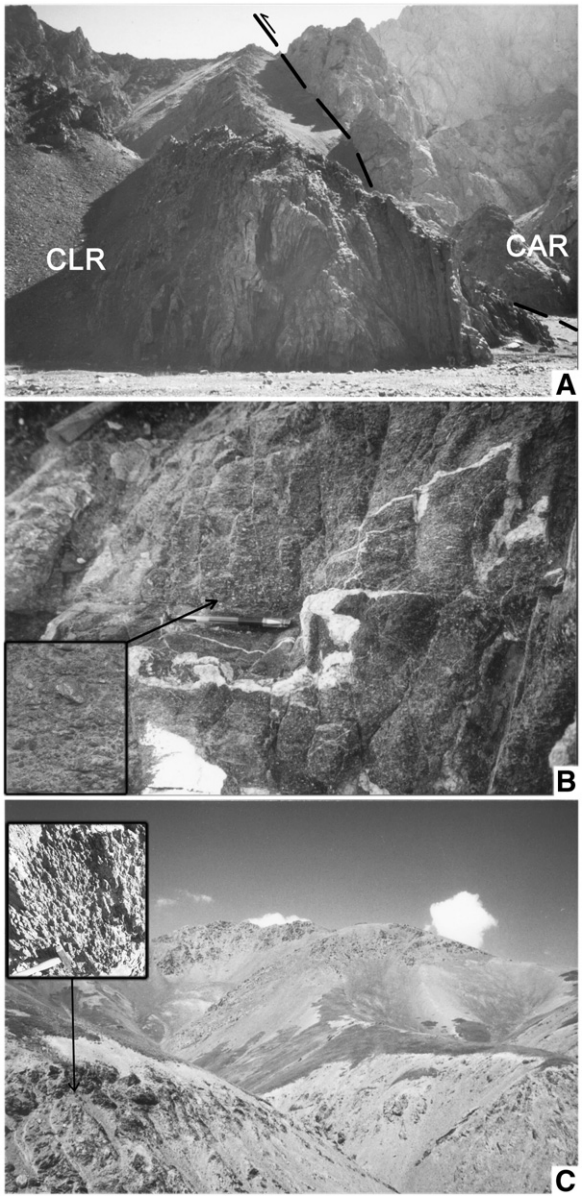

Fig. 2. Photographs of the large fault and fossil sampling locations. A. The clastic and the carbonate rock strata are separated by a large reverse fault presented with blue dashed line; B. The *Hapsiphyllide*, ostracoda, crinoidal nucha, algae, radiolaria samples were collected from thin-bedded marl and bioclastic limestone at the bottom of the lower segment in the ore-hosting strata; C. The *Schwagerina* samples were collected from pebbled sandstone and siltstone in the upper segment of the ore-hosting strata. The areas in the blue outlined box on the photographs show the expanded images of the arrowed areas. Abbreviations: CLR = clastic rock; CAR = carbonate rock.

The studied region hosts a number of well developed faults and folds, extending for several tens to several hundreds of km from NE to SW. The Sawaya'erdun gold deposit occurs as a sandwich between the Ariktoru reverse thrust fault in the east and the Yirkshtan thrust fault in the west. These major structures not only control the distribution of the strata in the region, but they also play an important role in regional metallogenesis (Zheng et al., 1996, 2001).

There are no large intrusive massifs in the area. However, some diorite dykes and diabase dykes in the west and south of the mining district are positioned within ore-hosting rocks and underlying strata. All these dykes strike NNE or close to N–S. In accordance with their geological and geochemical characteristics, these dykes are products of at least two different phases of tectonism (Zheng et al., 2001, 2002; Liu et al., 2002a): (i) Early Indosinian; K–Ar isotopic ages of the dykes were 207.5±4.2 to 187±18 Ma; and (ii) Early Yanshanian, K–Ar isotopic ages of 164.4±2.6 to 137.9±3.8 Ma, which is also consistent with the zircon U–Pb ages of 133.7 to 131.0 Ma given by Chen and Li (2003) for monzonite porphyry in this region.

3. Geological characteristics of the deposit

3.1. Ore zones and orebodies

The Sawaya'erdun gold district covers an area of about 27 km^2 and hosts several tens of fractured zones of different sizes. The fractured zones are roughly subparallel with the strata (Fig. 1). It has been proven that, within the mine district, all fractured zones are mineralized without exception. The 24 proven ore zones are significantly different in size, but the ore zone no. IV is the largest, with Au reserves exceeding 2.5 Moz (Liu et al., 1998a). The continuity of mineralization is best seen in ore zone no. IV, followed by ore zones nos. I, II, V and VI. The no. IV ore zone is 4200 m long and 15 to 48 m wide. Ore zones nos. I, II and IV are highly variable in size and are mainly stratoid, lenticular and vein-like in shape. The main orebody within ore zone no. IV measures 2870 m in length and up to 48 m in width over a vertical interval of 300 to 500 m. Typical gold grades are about 2 g/t, but can be much higher locally, up to 27 g/t. In addition to Au, grades of Ag, Sb and W are also relatively high. Silver grades are generally in the range 20 to 70 ppm, with a maximum of 1200 ppm. Tungsten grades attain as much as 150 ppm, and Sb concentrations can reach as much as 13 wt.%. The parts of some orebodies are effectively antimony ores and are located near the hanging wall in the middle and upper parts of the main orebody, coexisting with Au orebodies. Antimony orebodies are 180 to 340 m in length, and 2 to 10 m thick. The typical Sb grades are 1.09 to 2.35%.

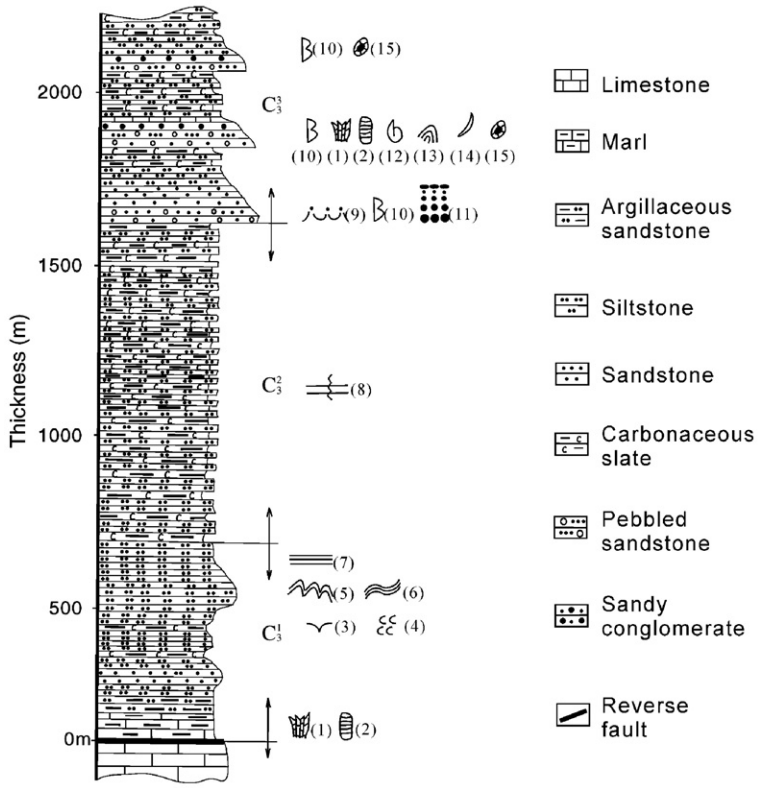

Fig. 3. Stratigraphic column of the ore-hosting clastic rock formation. (1) coral; (2) crinoidal nucha; (3) groove cast; (4) flute cast; (5) coiled bedding; (6) ripple lamination; (7) parallel bedding; (8) rhythmic stratification; (9) floor underwashing structure; (10) Bouma sequence; (11) graded bedding; (12) brachiopod; (13) alga; (14) ostracoda; (15) *Schwagerina*.

3.2. Mineralogy and ore types

The deposit is mineralogically complex. Until now, more than 30 minerals have been identified in the ores, including native elements, sulfides, sulfates and oxides of Au, Ag, Fe, Cu, Sb, As, Bi, Pb, Zn, Co, Sn, etc. (Figs. 4 and 5). The most common ore minerals are arsenopyrite, pyrite, marcasite, pyrrhotite, chalcopyrite, jamesonite, stibnite, sphalerite, galena, freibergite, berthierite, skutterudite, bismuthinite, native bismuth, electrum and native gold; gangue minerals are mainly quartz and siderite, with minor calcite and cassiterite. Owing to intense surface oxidation, secondary oxides are also extensively developed. The most important are goethite, lepidocrocite, malachite, anglesite, fibroferrite, jarosite and scorodite.

According to ore mineral assemblages, primary ores can be divided into six types: (1) gold-pyrite-quartz ore (Fig. 6A, B); (2) gold-arsenopyrite-pyrite-quartz ore (Fig. 6C, D); (3) gold-pyrite-pyrrhotite-quartz ore (Fig. 6E); (4) gold-pyrite-chalcopyrite-sphalerite-galena ore (Fig. 6F); (5) gold-jamesonite-stibnite ore (Fig. 6G); and (6) gold-siderite-calcite ore (Fig. 6H).

3.3. Wall-rock alteration

Wall-rock alteration in the deposit is mainly developed along and in the vicinity of mineralized fracture zones. Alteration types include silicification, pyritization, carbonatization, sericitization, and chloritization; the first two are dominant. Gold mineralization, for the most part, was emplaced in loci where silicification and pyritization are most intense. The outstanding feature of silicification is that the color of the rocks turned from dark- to light-gray, or even grayish-white, because organic matter was removed. Sericitization and carbonatization are widely distributed within carbonaceous slates of the mineralized fractured zone. Sericite is distributed along schistosity fissures and coexists with quartz. Sometimes, it is concentrated near quartz veinlets and is hard to distinguish from sericite formed as a result of regional metamorphism. However, it is relatively coarse and coexists with other alteration minerals such as pyrite and quartz. Generally speaking, wherever wall-rock alteration is intensely developed, sulfides and gold mineralization is abundant. Where wall-rock alteration is weak, sulfides are less abundant and gold grades are lower.

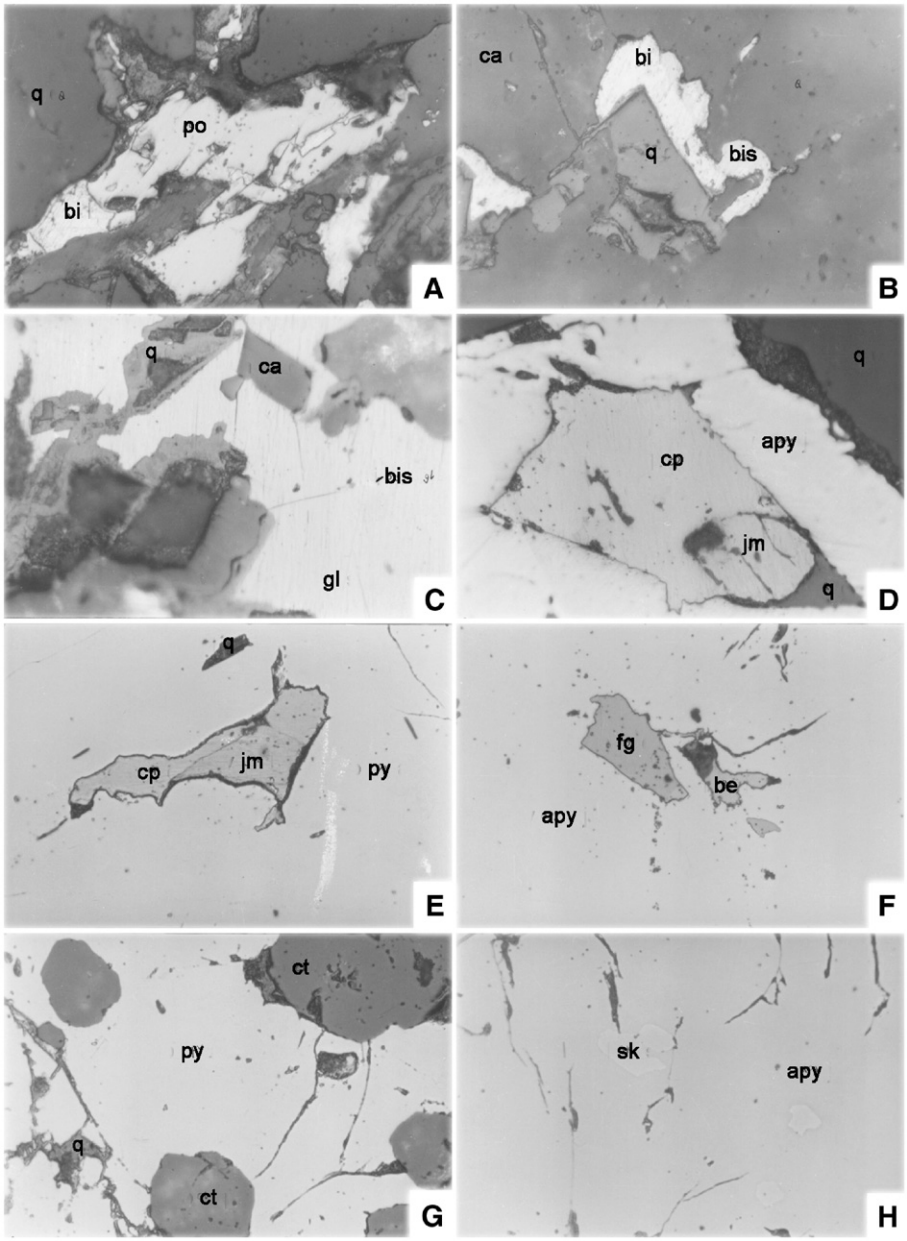

Fig. 4. Photomicrographs of mineral assemblages from Sawaya'erdun. All photomicrographs are in reflected light. Diagonal length of view is 0.19 mm. A. Native bismuth is closely associated with pyrrhotite and quartz. Sample S042-1; B. Native bismuth is closely in coexistence with bismuthinite. Sample S042-1; C. Bismuthinite coexists with galena, quartz and calcite. Sample S036-1; D. Jamesonite coexists with chalcopyrite and quartz in arsenopyrite. Sample S038-3; E. Jamesonite coexists with chalcopyrite and quartz in pyrite. Sample S039-1; F. Freibergite coexists with berthierite and pyrite. Sample S040-1; G. Granular cassiterite in pyrite. Sample S042-4; F. Skutterudite in arsenopyrite. Sample S042-5. Abbreviations: py = pyrite; apy = arsenopyrite; cp = chalcopyrite; po = pyrrhotite; gl = galena; be = berthierite; fg = freibergite; jm = jamesonite; bi = native bismuth; bis = bismutinite; ct = cassiterite; sk = skutterudite; q =quartz; ca = calcite.

3.4. Ore texture and structure

There exist various ore textures (Fig. 7), including (1) euhedral, subhedral and anhedral granular and mosaic textures formed as a result of crystallization; (2) replacement, replacement remnant, pseudomorphous and network textures resulting from metasomatism and filling; (3) microscopic girdles and colloidal textures formed by

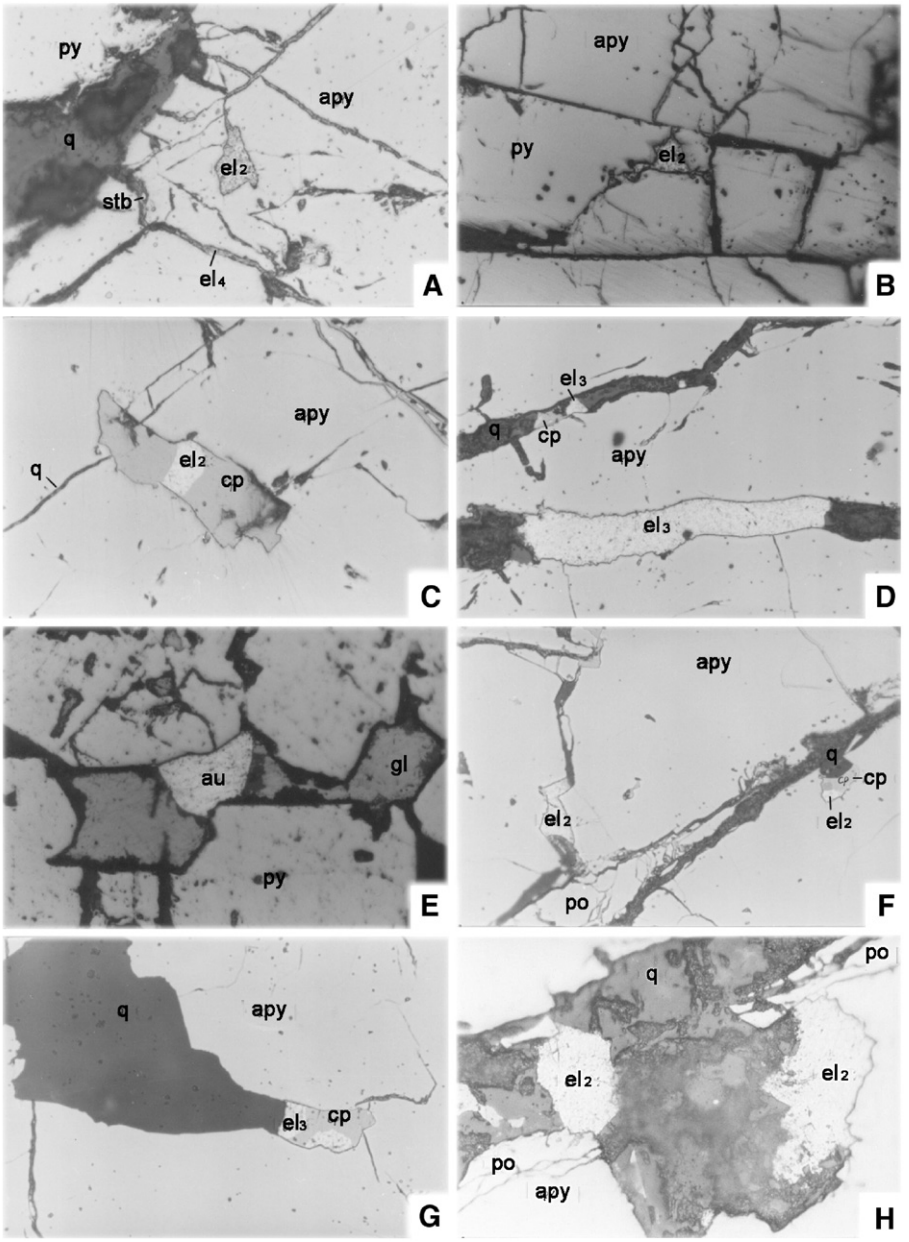

Fig. 5. Photomicrographs of gold association from Sawaya'erdun. All photomicrographs are in reflected light. Diagonal length of view is 0.19 mm. A. Electrum from the mineralization stage II (el2, hosted by arsenopyrite) and mineralization stage IV (el4, fracture-hosted by stibnite-quartz veinlet) Sample S042-2; B. Electrum from the mineralization stage II (el2, hosted by pyrite). Note the sharp boundary between pyrite and arsenopyrite. Sample S032; C. Electrum from the mineralization stage II (el2, hosted by chalcopyrite). Sample S042-10; D. Electrum from the mineralization stage III (el3, fracture-hosted by chalcopyrite-quartz veinlet). Sample S041-2; E. Native gold from mineralization stage III, which is closely in coexistence with pyrite and galena. Sample 99SW-23; F. Electrum from the mineralization stage II (el2, fracture-hosted by chalcopyrite-pyrrhotite-quartz veinlet). Sample S039-8; G. Electrum from the mineralization stage III (el3, fracture-hosted by chalcopyrite-quartz veinlet). Sample S037-1; H. Electrum from the mineralization stage II (el2), which is closely in coexistence with arsenopyrite, pyrrhotite, and quartz. Sample 99SW-25. Abbreviations: py = pyrite; apy = arsenopyrite; cp = chalcopyrite; po = pyrrhotite; gl = galena; stb = stibnite; el = electrum; au = native gold; q = quartz.

colloidal processes; (4) mortar and cataclastic textures formed under the action of stress. On a larger scale, a rough zoning with respect to ore structure (brecciation → fracturing → veining → dissemination) can be recognized from the center of the orebody outwards. All ore textures and structure are observed in each ore type.

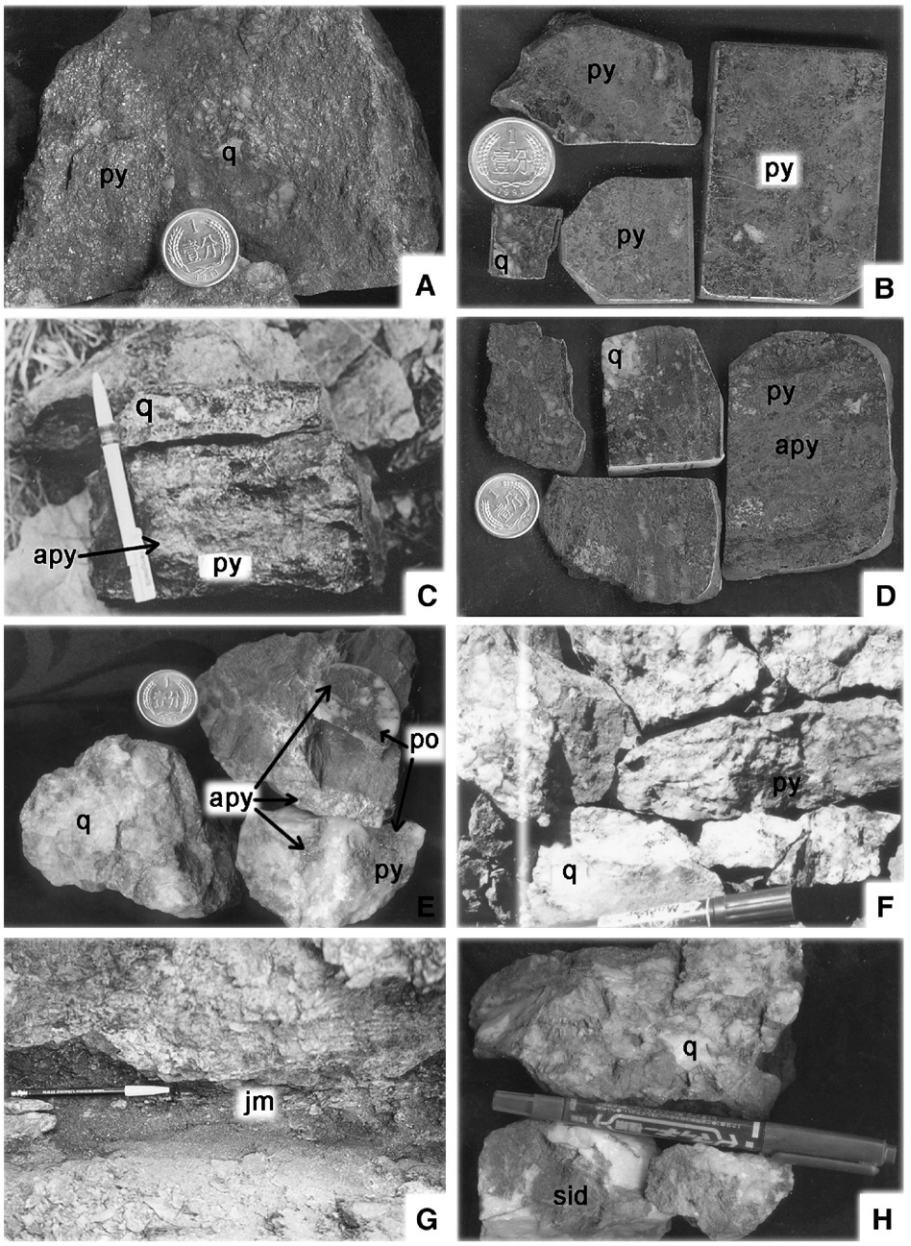

Fig. 6. Photographs of ore structures and ore types. A. Disseminated ore; B. Massive ore; C and D. Banded ores, with alternating yellow-white pyrite, dark-grey arsenopyrite and/or white quartz band; E. Quartz-sulfide vein, veinlet and stockwork ore; F. Quartz-cemented breccia vein ore, disseminated sulfide-bearing. G. Jamesonite vein and brecciated ore; H. Quartz-siderite vein ore, disseminated by pyrite. Abbreviations: py = pyrite; apy = arsenopyrite; po = pyrrhotite; jm = jamesonite; q = quartz; sid = siderite.

3.5. Gold association

Gold in the ore is present chiefly in the following forms: firstly as independent minerals (Fig. 5) in primary ores, especially sulfide-rich massive ores, in which we have found large quantities of electrum and native gold, coexisting with pyrite, arsenopyrite, chalcopyrite and quartz. Gold is particularly closely associated with chalcopyrite. Under the microscope, electrum and native gold, together with chalcopyrite and quartz, commonly constitute veinlets and networks penetrating arsenopyrite or pyrite. Occasionally, native gold and electrum occur independently as micro-fine veinlets (Fig. 5A). Secondly, gold is mechanically incorporated into host

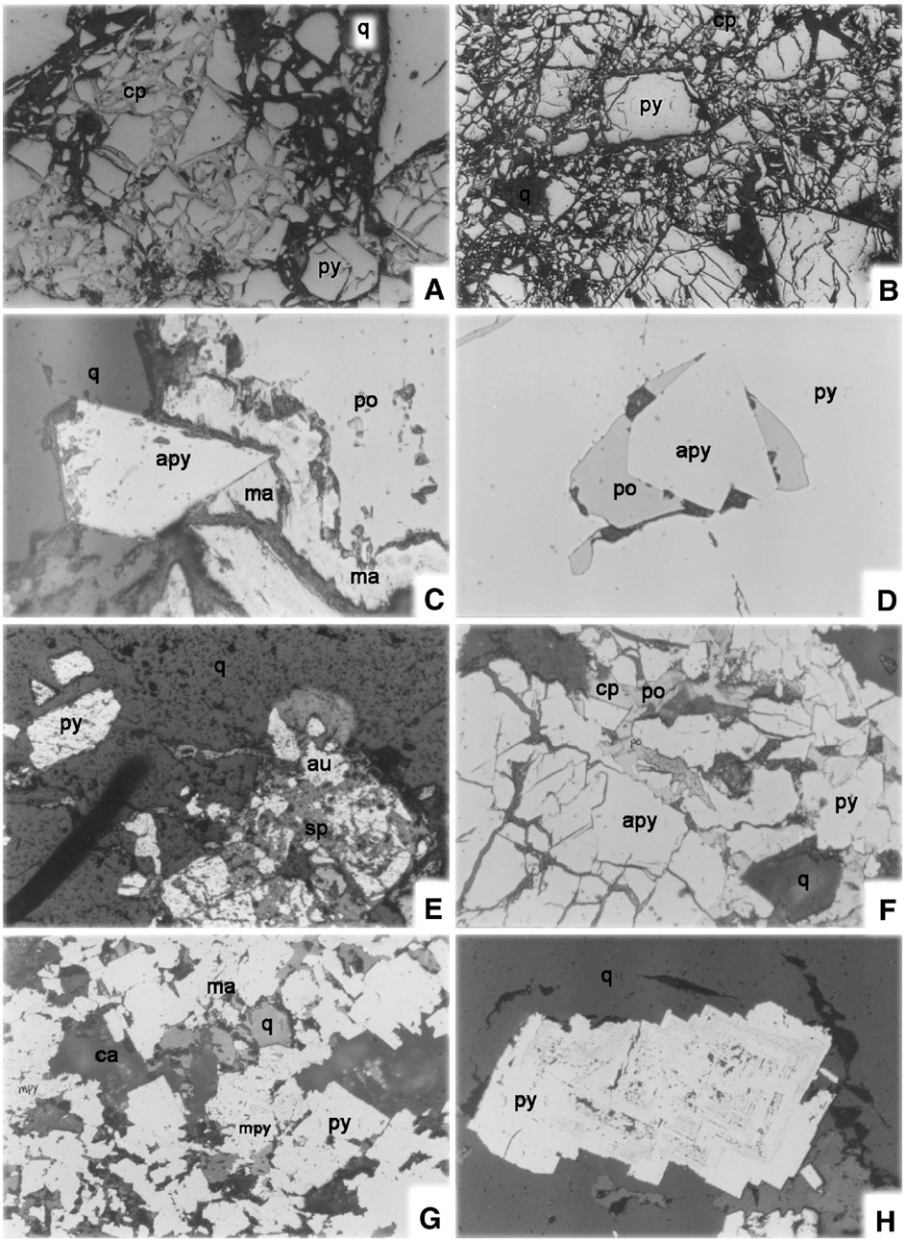

Fig. 7. Photographs of ore textures from the Sawaya'erdun gold deposit. All photomicrographs are in reflected light. A. Fracture crosscutting pyrite contains chalcopyrite and quartz, commonly constituting microfracture network texture. Diagonal length of view is 0.19 mm. Sample S042-10; B. Fracture crosscutting pyrite contains chalcopyrite and quartz, commonly constituting microfracture network and girdling textures. Diagonal length of view is 0.38 mm. Sample S041-2; C and D. Arsenopyrite, together with pyrrhotite and pyrite/marcasite, constitute euhedral, subhedral and anhedral granular textures formed as a result of crystallization. Diagonal length of view is 0.19 mm. Sample S042-1; E. Sphalerite replaces pyrite. Diagonal length of view is 0.38 mm. Sample S044; F. Chalcopyrite and pyrrhotite replace arsenopyrite and pyrite. Diagonal length of view is 0.38 mm. Sample S039-2; G. Melnikovite-pyrite and marcasite aggregate, showing colloidal texture. Both formed at equilibrium with respect to each other. Diagonal length of view is 0.19 mm. Sample S042-2; H. Ring fibre texture of pyrite in quartz. Diagonal length of view is 0.76 mm. Sample S041-2. Abbreviations: apy = arsenopyrite; py = pyrite; mp y= melnikovite-pyrite; ma = marcasite; cp = chalcopyrite; po = pyrrhotite; sp = sphalerite; au = native gold; q = quartz; ca = calcite.

minerals. The most important host minerals are pyrite and arsenopyrite. Gold also can be present in the adsorbed form. Relatively high contents of gold in organic carbon-rich and oxide ores seem to be related to the strong capabilities of organic carbon and clay minerals to adsorb gold.

3.6. Stages of mineralization

Based on the relationships of ore veins, mineral assemblages, paragenetic sequence (Fig. 8) and ore fabrics, five stages of mineralization can be recognized: (1) Stage I, represented by the association of pyrite-quartz; (2) stage II, represented by the association of arsenopyrite-pyrite-chalcopyrite-pyrrhotite-electrum-quartz; (3) stage III, represented by the common association of arsenopyrite-pyrite-chalcopyrite-galena-sphalerite-stibnite-electrum-gold-quartz; (4) stage IV, represented by the association of jamesonite-stibnite-quartz-gold; and (5) stage V, represented by the association of pyrite-siderite-calcite. Stages II, III and IV are the main stages and took place during the Indosinian epoch at 187~213 Ma (Liu et al., 2002b, 2004a).

4. Age of host rocks

The age of carbonate formation is generally thought to be Middle Devonian (Zheng et al., 1996; Wang et al., 2000). No unanimous conclusion can be drawn about the age of the clastic rock formation, but Li and Luo (1997), D. Liu et al. (1998a), Ye et al. (1998, 1999a), and Yang et al. (1999) have proposed a Silurian and Devonian age. We have undertaken Rb–Sr and Sm–Nd isotopic analysis and investigation of fossil records in order to provide new constraints on the age of the ore-hosting strata.

Minerals	Stage I	Stage II	Stage III	Stage IV	Stage V
pyrite	▬▬	▬▬	▬	—	▬▬
arsenopyrite		▬▬	▬▬		
chalcopyrite		▬▬	▬▬		
pyrrhotite		▬▬	▬▬		—
galena			▬▬		
sphalerite			▬▬		
jamesonite			—	▬▬	
stibnite			—	▬▬	
marcasite	—	▬▬	▬▬		
native gold		▬▬	▬▬	—	—
electrum		▬▬	▬▬	—	—
melnikovite-pyrite		—	▬▬		
freibergite			—		
berthierite			—		
native bismuth			—		
bismuthinite			—		
skutterudite		—	—		
galenobismutite			—		
cassiterite		—			
quartz	▬▬	▬▬	▬▬	▬▬	
siderite					▬▬
calcite					▬▬

Fig. 8. Paragenetic sequence of main minerals from the five mineralization stages. Width of lines corresponds to the relative abundance of minerals of each stage.

4.1. Collection, pulverization and analysis of samples

Whole rock samples for Sm–Nd and Rb–Sr isochronal methods were collected from strata section a–b and c–d (Fig. 1); the weight of each sample was generally about 1 kg. In order to take account of samples altered by late hydrothermal fluids, these samples were cut and then studied under a microscope. Rock samples with the same fabric and mineral associations were chosen and pulverized to <200 mesh (<0.093 mm); this material was then analyzed. Both chemical separation and mass-spectrometric determinations were conducted at the Yichang Institute of Geology, Chinese Academy of Geological Sciences and the Modern Analysis Center of Nanjing University, using high-pressure-cover-melting and positive-ion-exchange techniques with the aid of MAT-261 and VG-354 isotopic mass spectrometer, respectively.

The $^{87}Sr/^{86}Sr$ ratio of American isotopic standard (NBS987) is determined as $0.710389 \pm 9(2\sigma)$. The relative deviation is less than 0.015% compared to the credential value (0.71034 ± 26). Background values of Sr and Rb in the whole experiment are 0.20×10^{-9} g and 0.3×10^{-9} g, respectively. The $^{143}Nd/^{144}Nd$ ratio of the American La Jolla isotopic standard is $0.511860 \pm 6(2\sigma)$. The relative deviation is less than 0.015% compared with the credential value (0.512633 ± 4). The basal value of Nd in the whole process is $(5–7) \times 10^{-11}$ g. The ratios $^{86}Sr/^{88}Sr = 0.1194$ and $^{146}Nd/^{144}Nd = 0.7219$ were used to calibrate isotopic values of $^{87}Sr/^{86}Sr$ and $^{143}Nd/^{144}Nd$. Analytic errors of $^{87}Sr/^{86}Sr$ and $^{143}Nd/^{144}Nd$ (2σ) were ±1% and ±2%, respectively. Rb–Sr and Sm–Nd isochron ages were calculated using the Ludwig (1996) ISOTOPE Program (Version 2.90) with 2σ index for dating error and $\lambda_{Rb} = 1.42 \times 10^{-11}$ a^{-1} and $\lambda_{Sm} = 6.45 \times 10^{-11}$ a^{-1}. The double-error regression method (York, 1969) is used in calculating Rb–Sr and Sm–Nd isochron age. Errors on reported ages are given as 2σ.

The fossils were identified by Professors Shi Yan, Duan Lilan and Gou Zonghai of the Paleontology Section, Chengdu University of Technology.

4.2. Results and discussions

4.2.1. Rb–Sr and Sm–Nd isotope ages

Before an abundance of index fossils were found, we tried to obtain a reliable recognition of the ore-hosting strata using Rb–Sr and Sm–Nd isotope geochronology. Five carbonaceous slate samples (S-009, 011, 013, 014, and 020), five chert samples (98s-20, 31, 33 and 97a-74) and one sandstone sample (98s-32) were selected. Results of whole rock Rb–Sr and Sm–Nd isotopic

Table 1
Results of Rb–Sr isotopic analyses for the whole rock of carbonaceous slates, sandstone and chert from the Sawaya'erdun gold deposit

No.	Sample no.	Lithology	$Rb/10^{-6}$	$Sr/10^{-6}$	$^{87}Rb/^{86}Sr$	$^{87}Sr/^{86}Sr$ ($\pm 2\sigma$)
1	S-009	Carbonaceous slate	213.06	131.01	4.6990	0.73104±0.00001
2	S-011	Carbonaceous slate	140.69	157.03	2.5868	0.72297±0.00001
3	S-013	Carbonaceous slate	202.71	192.16	3.0462	0.72436±0.00001
4	S-014	Carbonaceous slate	236.47	178.99	3.8166	0.72882±0.00001
5	S-020	Carbonaceous slate	296.19	107.39	7.9811	0.74630±0.00001
6	98s-20	Black chert	25.35	95.76	0.7809	0.713750±0.000014
7	97a-74	Gray-green chert	51.48	25.33	5.5720	0.733705±0.000019
8	98s-32	Pyrite-bearing sandstone	63.26	21.29	6.9980	0.739617±0.000022
9	98s-33	Pyrite-bearing chert	223.4	339.1	1.9470	0.718623±0.000025
10	98s-31	Black chert	84.82	79.03	3.1560	0.723134±0.000016

Samples 1–5 samples were analyzed at the Yichang Institute of Geology, CAGS; Samples 6–10 samples were analyzed at the Modern Analysis Center, Nanjing University.

analysis are presented in Tables 1 and 2 and depicted in Figs. 9 and 10.

In the host rocks of the gold deposit, ratios of $^{87}Rb/^{86}Sr$ from carbonaceous slates range from 2.5868 to 7.9811; ratios of $^{87}Sr/^{86}Sr$ range from 0.72297 to 0.74630. We have done a York best-fit analysis of the Rb–Sr isotope data (Fig. 9A). The calculated slope of this line is 0.004335±0.000166, giving an isochron age of 304.7± 11.6 Ma. In contrast, however, $^{87}Rb/^{86}Sr$ ratios from cherts and pyrite-bearing sandstones very from 0.7809 to 6.9980; corresponding $^{87}Sr/^{86}Sr$ ratios range from 0.713750 to 0.740134. Our York best-fit analysis of this data (Fig. 9B) gives a calculated slope of 0.00416± 0.00005 and an isochron age of 292.43±0.38 Ma.

In the host rocks of the gold deposit, $^{147}Sm/^{144}Nd$ ratios of cherts and pyrite-bearing sandstones range from 0.06573 to 0.1621 and $^{143}Nd/^{144}Nd$ values range from 0.511948 to 0.512530. We have done a York best-fit analysis of the Sm–Nd isotope data (Fig. 10). The calculated slope of this line is 0.001927±0.000125, giving an isochron age of 294±19 Ma. This age is similar to that obtained by Rb–Sr methods (Fig. 9).

When attempting to constrain diagenetic or hydrothermal events using isotopic systems, the different isotopic systems each carry a set of unique implications due to variation in closure temperatures. Closure temperatures for Rb–Sr and Sm–Nd isotopic systems for the whole rock are equal or greater than 650 °C (Dodson, 1976; Humphrises and Cliff, 1982; Hollister, 1982; Cliff et al., 1985; Wang et al., 1988; Li, 1996; Fang et al., 2001). Although ages of carbonaceous slates and sandstones by Rb–Sr and Sm–Nd isochronal methods probably reflect a close-to-peak metamorphic age, cherts are more likely to be reset after closure of their isotopic systems. Generally speaking, isotopic ages of cherts were not reset during the later low-grade metamorphism in the area (Knauth and Epstein, 1976; Jiang, 1989). Therefore, we suggest that ages determined by the Rb–Sr and Sm–Nd isochronal method from the chert might have probably represented the time of sedimentation and/or diagenesis. However, this age is also consistent with mineralization age at Muruntau and Kumtor (Mao et al., 2004).

4.2.2. Fossil age

Since 1995, fossils of algae, radiolaria, brachiopoda, ostracoda, crinoidal nucha, corals and *Schwagerina* have been found in the ore-hosting strata (Liu et al., 1999). Corals, *Schwagerina* and brachiopoda (Fig. 11) are the most useful fossils to provide age data. The coral is characterized by developed septal fossula and parietes symmetrical pinnate arrangement (Fig. 11A). It belongs to *Hapsiphyllide* Grabau, 1928, and is typical for the Upper Carboniferous to Lower Permian (Yu et al., 1983). On the adjoining sagittal section of *Schwagerina*, an alveolar

Table 2
Results of Sm–Nd isotopic analyses for the whole rock of sandstone and chert from the Sawaya'erdun gold deposit

Serial No.	Sample No.	Lithology	$Sm/10^{-6}$	$Nd/10^{-6}$	$^{147}Sm/^{144}Nd$	$^{143}Nd/^{144}Nd$ ($\pm 2\sigma$)
1	98s-20	Black chert	8.369	46.82	0.1077	0.512028±0.000008
2	97a-74	Gray-green chert	3.017	11.26	0.1621	0.512134±0.000010
3	98s-32	Pyrite-bearing sandstone	5.028	26.98	0.1136	0.512039±0.000011
4	98s-33	Pyrite-bearing sandstone	2.796	25.74	0.06573	0.511948±0.000007
5	98s-31	Pyrite-bearing sandstone	9.813	49.05	0.01214	0.511835±0.000016

Samples were analyzed at the Modern Analysis Center, Nanjing University.

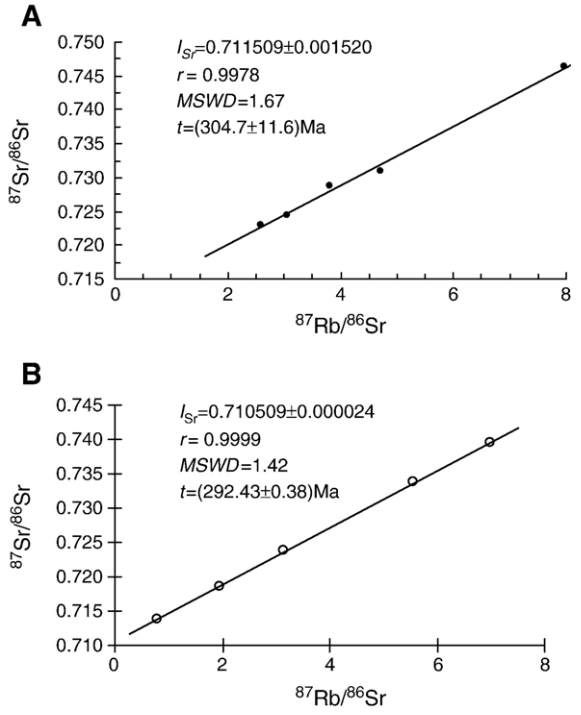

Fig. 9. The whole rock Rb–Sr isochron of the ore-hosting strata from the Sawaya'erdun gold deposit. A. The Rb–Sr isochronal line of carbonaceous rocks; B. The Rb–Sr isochronal line of the cherts and pyrite-bearing sandstones.

texture is observed (Fig. 11B). Although *Schwagerina* is widely distributed in the Upper Carboniferous and Lower Permian, *Schwagerinidae* is an index fossil for the Upper Carboniferous (Tan, 1983). The brachiopoda (Fig. 11C) are small (~10 to 13 mm) and are characterized by circular or pentagonal forms, small and hook umbone, slight carina of brachial valve, severe convexity of ventral valve, big notothyrium, narrow notodeltidium, flat dorsal face, low or no median fold, shallow or no median sinus, smooth face or accidentally concentric ornamentation in hull. They belong to *Crurithyris speciosa*, Wang and *Crurithyris cf. speciosa*, Wang, whose strata range is Upper Carboniferous to Lower Permian (Tan, 1983). Because *Hapsiphyllide* occurs in thinly-bedded marl and bioclastic limestone at the bottom of the lower segment

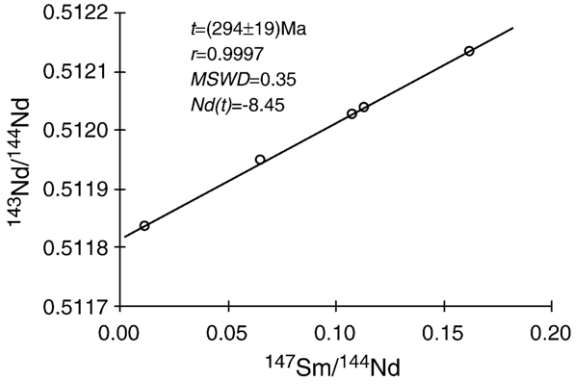

Fig. 10. The whole rock Sm–Nd isochron of the cherts and pyrite-bearing sandstones from the Sawaya'erdun gold deposit.

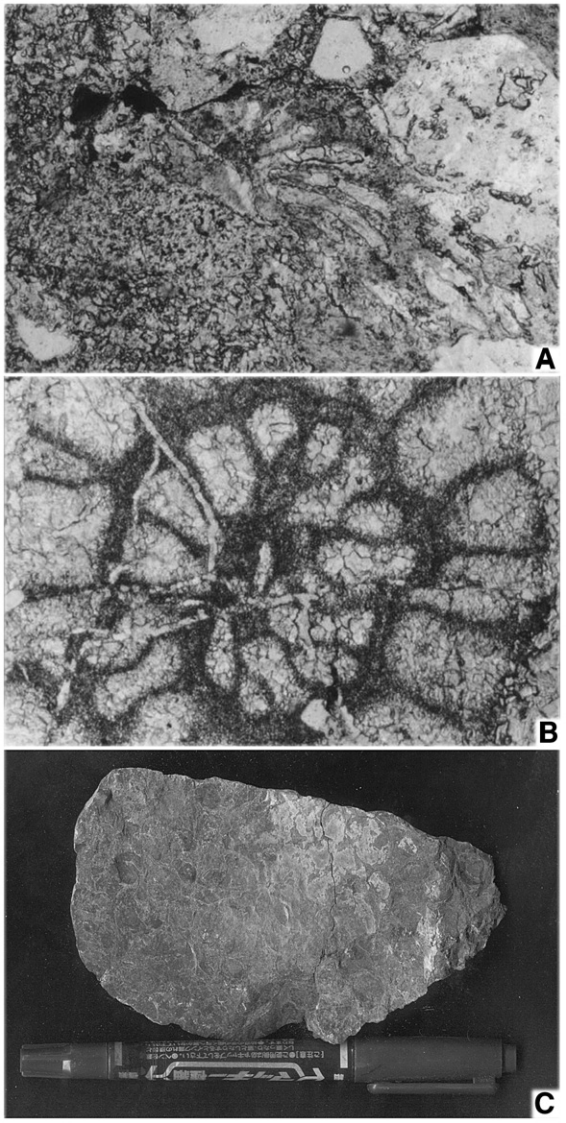

Fig. 11. The index fossil organisms in the ore-hosting strata. A. *Hapsiphyllide* from limestone in the lower ore-hosting strata. Thin section in plane-polarized light, 3.8 mm diagonal field of view. Sample S002; B. *Schwagerinidae* from pebbled sandstone in the upper ore-hosting strata. Thin section in plane-polarized light, 3.8 mm diagonal field of view. Sample S079; C. *Crurithyris speciosa,* Wang and *Crurithyris cf. speciosa*, Wang from siltstone in the upper ore-hosting strata. Sample 99SW-65.

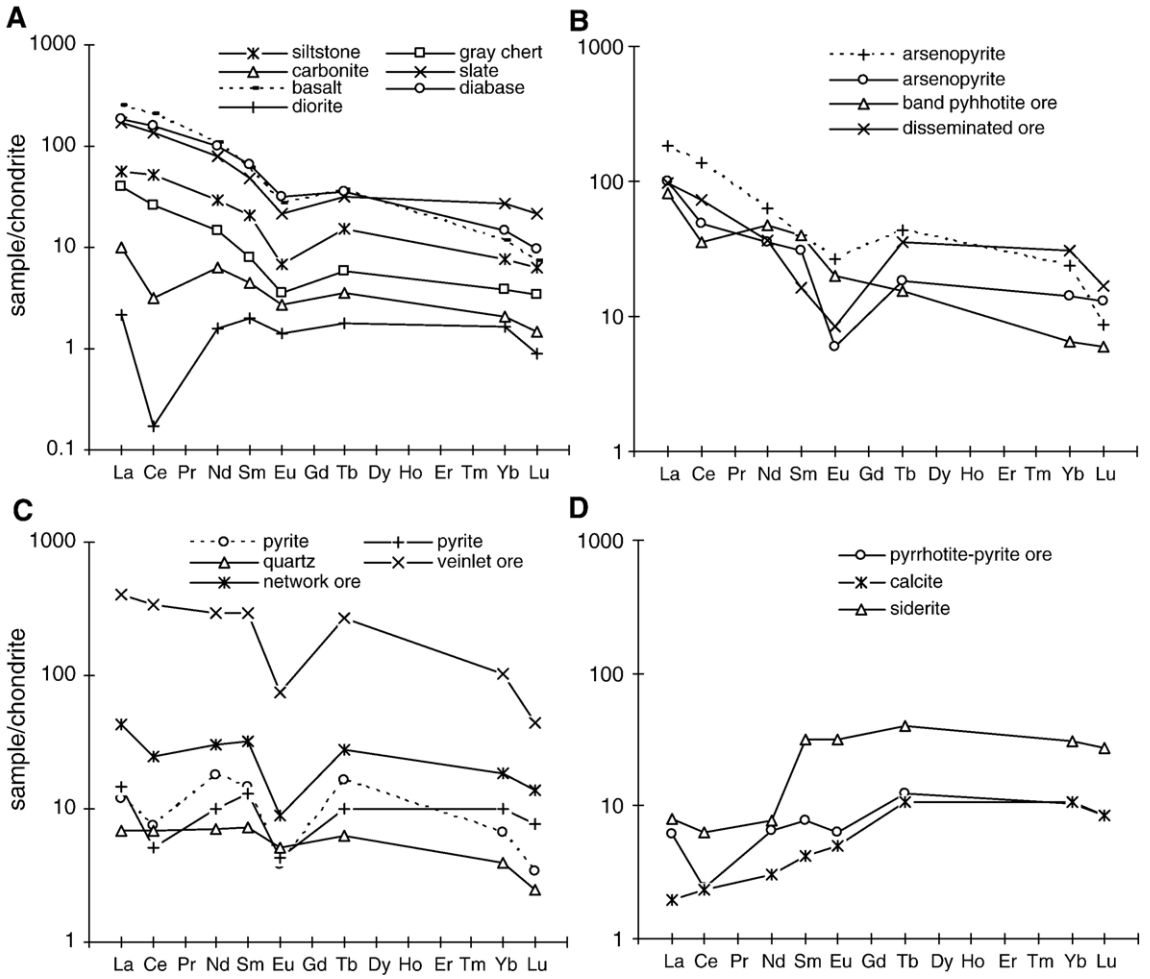

Fig. 12. Chondrite-normalized REE pattern of rocks, ores and hydrothermal minerals in the Sawaya'erdun deposit.

(Fig. 2B), and *Schwagerina*, brachiopoda occurs in pebbled sandstone and siltstone from the upper segment of the ore-hosting strata (Fig. 2C), the fossil age may be earlier than that of the fossil-bearing strata.

Combining the Rb–Sr and Sm–Nd age data with the information from the fossil record, we suggest that the ore-hosting strata probably belong to the Upper Carboniferous rather than to the Silurian, Devonian (Li and Luo, 1997; Ye et al., 1999a; Wang et al., 2000), or even Precambrian as had been suggested earlier (Liu et al., 1998a).

5. Geochemical methodology

Seven hundred fifty two host rock, mineralized rock and ore samples were collected along sections a–b and c–d (Fig. 1), from exploration trenches from shallow pits, drill holes and from the orebodies. Fresh quartz veins were sampled for $^{40}Ar/^{39}Ar$ fast neutron activation and Rb–Sr isochronal analysis from ore zones nos. I and IV. Firstly, polished thin sections and double-polished inclusion sections were prepared. These were studied under the microscope to determine the extent of alteration, to investigate mineral assemblages, ore textures and inclusion characteristics. In accordance with the microscopic observations, typical rock, mineralized and ore samples were selected and ground to −200 mesh. The selected ore minerals and gangue minerals were crushed, sieved and handpicked until grain size reached 40–60 mesh, and the purity exceeded 98%. The ground quartz sample was then immersed in 5% dilute HNO_3 for one hour to remove minor amounts of calcite. Finally, the pre-treated sample was repeatedly washed in clean and distilled water and then dried at 80 °C.

Various analyses and measurements were conducted on the selected samples. For the sake of understanding

the trace and rare earth element (REE) geochemistry of the deposit, neutron activation analyses were conducted on 93 rock, ore and hydrothermally-altered samples. Trace elements and REE contents were analyzed at the Laboratory of Neutron Atomic Activation (NAA), Chengdu University of Science and Technology (CUST). In order to estimate ore-formation temperature, the homogenization temperatures and salinities of fluid inclusions were measured by the senior author at the Laboratory of Ore Deposits, CUST, and the key Laboratory of Ore Deposit Geochemistry, Chinese Academy of Sciences (CAS). In order to constrain the sources of ore-forming material and age of mineralization, various isotopic measurements were undertaken at the Stable Isotope Laboratory, Institute of Mineral Resources, at the Isotope Analysis Center of the Yichang Institute of Geology and Mineral Resources, Chinese Academy of Geological Sciences (CAGS), at the Key Laboratory of Ore Deposits Geochemistry and at the State Key Laboratory of Environmental Geochemistry, Institute of Geochemistry, CAS, and at the Isotope Laboratory, Institute of Geology and Geophysics, CAS. Analytical methods are described below.

For S-isotope analyses, Cu_2O was used as the oxidizer for preparation of sulfide samples. Sulfate minerals were purified to pure $BaSO_4$ by the carbonate-zinc oxide semi-melt method, and then SO_2 was prepared by the V_2O_5 oxide method. VCDT standard material was used. For O and C isotope analysis, calcite and siderite were reacted with phosphoric acid at 25 °C (McCrea, 1950) to release CO_2. Two Chinese national standards of carbonate for C and O isotopes, GBW04416 and GBW04417, were used as working standards in experiments. The $\delta^{13}C_{PDB}$ and $\delta^{18}O_{PDB}$ values of GBW04416 determined by NBS-19 were 1.6 and −11.6‰, respectively. The $\delta^{13}C_{PDB}$ and $\delta^{18}O_{PDB}$ values of GBW04417 were −6.1 and −24.1‰, respectively. The $\delta^{18}O_{PDB}$ values of calcite and siderite samples were directly obtained from $\delta^{18}O$ values of their CO_2 against the CO_2 of PDB. To convert $\delta^{18}O_{PDB}$ to $\delta^{18}O_{SMOW}$, the equation by Friedman and O'Neil (1977) was used,

$$\delta^{18}O_{SMOW} = 1.03091 \times \delta^{18}O_{PDB} + 30.91$$

For oxygen isotope analysis of silica and silicates, CO_2 was prepared by the BrF_5 method described by

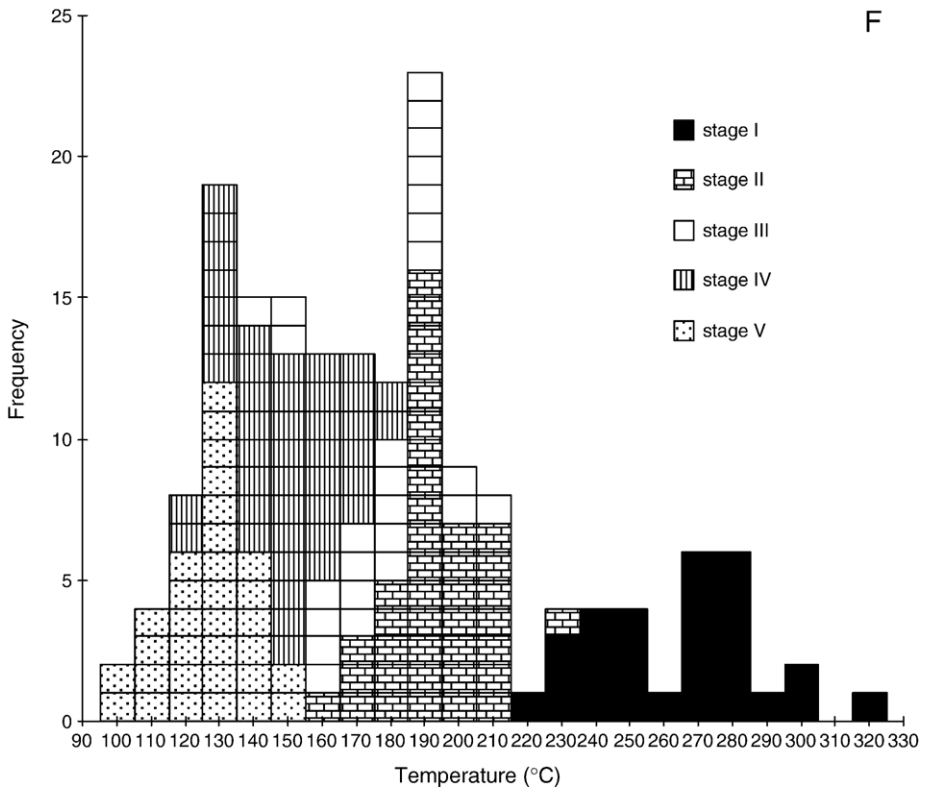

Fig. 13. Histogram showing homogenization temperature of fluid inclusions in the Sawaya'erdun deposit. A. Mineralization stage I; B. Mineralization stage II; C. Mineralization stage III; D. Mineralization stage IV; E. Mineralization stage V; F. All mineralization stages.

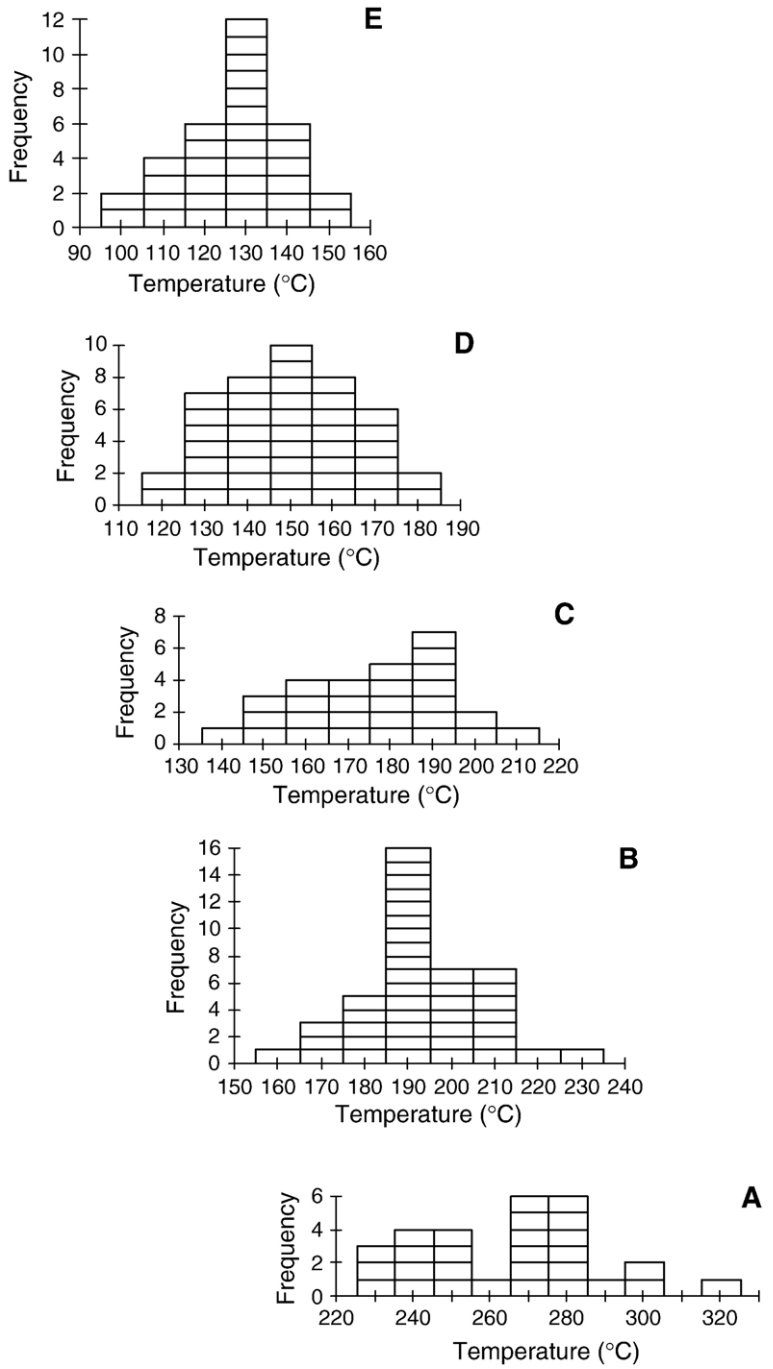

Fig. 13 (*continued*).

Clayton and Mayeda (1963). For H isotope analysis, the water in fluid inclusions was released by decrepitation method. Then the water was reacted with Zn at 400 °C to produce H_2 (Coleman et al., 1982), which was collected in sample tube with active charcoal at liquid N_2 temperature.

Silicon was extracted from samples by fluorination involving reaction with BrF_5 at 550 to 600 °C to produce SiF_4 gas (Ding et al., 1994). The SiF_4 gas was purified by liquid N_2 and dry ice–acetone separation; it was then passed through a preheated Cu tube containing pure Zn particles to remove any remaining BrF_5. The

standard is NBS-28 quartz sandstone provided by the U.S. National Bureau of Standards and Technology. Measurements of quartz sandstone standard NBS-28 gave average value of $\delta^{28}Si_{NBS-28}=0.00\pm0.06‰$.

All SO_2, SiF_4, CO_2 and H_2 analyses were obtained with a Finnigan MAT-251 mass spectrometer. Analytical precision was ±0.2‰ for C, O, and S isotopes, ±0.1‰ for Si isotopes, and ±2‰ for H isotopes.

For Pb isotope analysis, we used the sample pretreatment procedure described by Robin et al. (1999). Whole-rock samples (400 mg) were dissolved in a mixed HF, HCl and HBr solution; arsenopyrite, chalcopyrite, pyrite, pyrrhotite, stibnite and jamesonite (400 mg) were first washed with HCl to remove impurities coated on the mineral surfaces, then dissolved in aqua regia under heating, and finally converted to an HBr chromatographic solution. The Pb in solution was eluted using an ion exchange resin with HBr–HCl. Of 29 samples, 27 samples were used for analysis on a MAT-261 mass spectrometer and 2 samples on a VG-354 mass spectrometer. Of the samples, 20% was repeatedly analyzed. The fractionation factor (0.1% per atomic mass unit) is worked out in terms of the results of Pb isotopic analyses of NBS-981 as the international standard, so as to make correlations for the Pb isotopic ratios of the samples. Measurements of common-lead standard NBS-981 gave average values of $^{206}Pb/^{204}Pb=16.923\pm3$, $^{207}Pb/^{204}Pb=15.467\pm3$, $^{208}Pb/^{204}Pb=36.733\pm6$ for VG-354 and $^{206}Pb/^{204}Pb=16.924\pm3$, $^{207}Pb/^{204}Pb=15.468\pm3$, $^{208}Pb/^{204}Pb=36.732\pm6$ for MAT-261 with uncertainties <0.1% at the 95% confidence level. The bulk lead blanks for the whole procedure are <1 ng and analytical results for all samples are corrected for this. Duplicate analysis indicates similar reproducibility in all cases. The bulk error is <0.1% for lead isotopic samples.

The Rb–Sr mass spectrometric analysis of quartz fluid inclusions was conducted in accordance with the procedure of Li et al. (1993). The $^{87}Sr/^{86}Sr$ ratio determined for NBS987 is $0.710233\pm54(2\sigma)$. The relative deviation is less than 0.015% as compared with the credential value (0.71034±26). Background values of Sr and Rb in the whole experiment are 0.2×10^{-9} g and 0.3×10^{-9} g, respectively. The double-error regression method (York, 1969) is used in calculating Rb–Sr isochron age on quartz fluid inclusions.

Preparation of quartz samples and standard samples for analysis, fast neutron irradiation, incremental heating for Ar extraction and purification, and mass spectrometric analysis were all conducted in accordance with the procedure of Sang et al. (1994). Monomineralic samples were wrapped in aluminum foil and placed in the central part of the B8 hole site of the 49-2 Type reactor for fast neutron irradiation. Standard samples used to monitor neutron fluxes include ZBH-25 Biotite, ZBJ Hornblende from China and GA1550 Biotite from Australia, whose respective ages are 132.9±1.2 Ma, 132.8±1.4 Ma, and 97.6±0.6 Ma (Sang et al., 1994). Measurements were conducted on an RGA-10 gas source mass-spectrometer (VSS Co., U.K.). In static mode, the blanks of the whole system were determined as $^{40}Ar=1.6\times10^{-14}$ mol and $^{36}Ar=1.2\times10^{-16}$ mol. The decay constant λ is 5.543×10^{-10}/a. Errors involved in the Ar measurements are within the range 0.5 to 1%.

6. Results

6.1. REE contents and chondrite-normalized REE patterns

Because the chondrite-normalized REE distribution patterns of most samples share a number of common features, the authors selected the NAA results of some representative samples for discussion. Chondrite-normalized REE distribution patterns are shown in Fig. 12. Analytical results indicate that ΣREE in sedimentary and volcanic rocks vary over a relatively large interval from 2.7 to 328.9 ppm. With the exception of a single diorite sample, the sample suite is characterized by LREE/HREE>4, $(La/Yb)_N>4$, negative Eu anomalies (δEu=0.29 to 0.76) and unremarkable Ce anomalies (Fig. 12A). The slope for diabase and basalt [$(La/Yb)_N>13$] is, in particular, higher than that of the sedimentary rocks [$(La/Yb)_N=4.86$ to 8.53]. Total REE amounts in ores and hydrothermal minerals also are highly variable (8.49 to 222.1 ppm). In accordance with their REE distribution patterns, the samples can be divided into three groups. Samples of the first group (Fig. 12B) display strong LREE enrichment (LREE/HREE>14), with slopes $(La/Yb)_N$ of 4 to 8. For this group of samples, the extent of LREE fractionation [$(La/Sm)_N=3.27$ to 5.48] is greater than that of HREE fractionation [$(Tb/Yb)_N=1.3$ to 2.38]; negative Eu anomalies (δEu=0.37 to 0.84) are prominent. These features are, in many ways similar to REE distribution patterns in the sedimentary rocks, but in contrast to the volcanic rocks, $(La/Yb)_N$ exceeds 10. Samples of the second group (Fig. 12C) show weak LREE enrichment, with LREE/HREE between 6 and 12, nearly flat REE distribution pattern curves slope [$(La/Yb)_N=1.44$ to 3.93], remarkable Eu depletion (δEu=0.27 to 0.76), Ce depletion in most cases, and extents of LREE and HREE fractionation reaching $(La/Sm)_N=0.81$ to 1.39 and $(Tb/Yb)_N=0.83$ to 2.63, respectively. Samples of the third group are HREE-enriched (Fig. 12D). The samples with

such REE characteristics clearly are products of late-stage mineralization. Total REE is low (8.49 to 30.07 ppm), with LREE/HREE ratios of 1 to 3. Their slopes $(La/Yb)_N$ are shallow (0.18 to 0.59) and the extent of LREE fractionation [$(Tb/Sm)_N$=0.25 to 0.79] is lower than that of HREE fractionation [$(La/Yb)_N$= 1.17 to 2.46], with no remarkable negative Eu anomaly (δEu=0.65 to 0.99).

6.2. Fluid inclusion characteristics and estimation of ore-formation temperature

6.2.1. Fluid inclusion characteristics

Large numbers of fluid inclusions exist in transparent minerals such as quartz and calcite. General observations include the abundance of fluid inclusions in quartz relative to calcite, the greater number of highly-

Table 3
$\delta^{34}S$ values (‰) of major sulfides from the Sawaya'erdun gold deposit

No.	Sample No.	$\delta^{34}S_{-CDT}$ (‰)					Stages of mineralization
		Arsenopyrite	Pyrite	Pyrrhotite	Jamesonite	Stibnite	
1	S042-2	1.01					Stage II
2	SII-20-2	0.83					Stage III
3	SII-41	0.35					Stage III
4	SIV97-1			−0.12			Stage II
5	SIV97-2			−0.29			Stage II
6	S042-1		0.23				Stage II
7	SI-11		−0.09				Stage II
8	SII-20		0.18				Stage II
9	SII-20-2		0.27				Stage II
10	SII-41		0.16				Stage II
11	SII-42		0.24				Stage II
12	SII97-3		0.45				Stage II
13	SIV97-1-1		0.65				Stage II
14	SIV97-11		0.45				Stage II
15	SIV97-2		0.38				Stage II
16	SIV97-23-1		0.26				Stage II
17	SIV97-3		0.51				Stage II
18	SIV97-30		2.61				Stage II
19	SIV97-6		0.71				Stage II
20	SIV97-22					−1.35	Stage III
21	s0-70-1		−0.28				Stage III
22	s0-70-3-1		−0.19				Stage III
23	S045				−3.00		Stage IV
24	SII-19-1				−0.77		Stage IV
25	SII-19-2				−1.02		Stage IV
26	SIV97-27				−0.48		Stage IV
27	SIV97-23-2			0.25			Stage II
28	SIV97-1-2		0.71				Stage II
29	s0-70-3-2		−0.20				Stage III
30	SII-19-1				−1.02		Stage IV
31	sg23-1		1.10				Stage I
32	sg-25		0.50				Stage I
33	sw-12		−0.70				Stage I
34	iv-I-06		−1.90				Stage III
35	sk-01		−2.20				Stage III
36	4-27-02		0.20				Stage III
37	27kd-02		−0.90				Stage III
38	27kd-03		0.20				Stage III
39	tc-01		−0.20				Stage III
40	tc24-q1		−0.90				Stage III
41	tc24-q2		0.40				Stage III

Samples 1–26 were analyzed at the Isotope Analysis Center of the Yichang Institute of Geology and Mineral Resources, CAGS; Samples 27–30 were analyzed at the Key Laboratory of Ore Deposits Geochemistry, Institute of Geochemistry, CAS; data for the others (31–41) were published by Ye et al. (1999a).

transparent quartz inclusions, but smaller number of poorly-transparent quartz inclusions, that quartz inclusions formed during the main stage of metallogenesis are more numerous and larger in size than those formed during the late stage of metallogenesis. Inclusions in quartz are mostly elliptical, rounded, rectangular or irregular in shape and vary greatly in size (generally 3 to 15 μm). Inclusions in calcite are mostly rhomb-shaped and are generally small in size (2 to 6 μm).

Three major types of fluid inclusions have been distinguished: gas-liquid, liquid, and CO_2-rich. Gas-liquid and liquid inclusions are all composed of water and vapor, of which vapor accounts for 3 to 30% of the total volume. When heating, the vapor phase disappears and homogenizes to liquid. The CO_2-rich three-phase inclusions are composed of liquid CO_2, gaseous CO_2 and liquid H_2O, of which CO_2 accounts for 5 to 7% of the total inclusion volume. When heated, CO_2 disappears in most cases and homogenizes to aqueous solution; some inclusions decrepitate before reaching homogenization (Long et al., 1998).

6.2.2. Homogenization temperatures

We systematically measured homogenization temperatures of inclusions in hydrothermal minerals such as quartz and calcite. Results are 110 to 320 °C for quartz and 100 to 150 °C for calcite. In accordance with the occurrence characteristics of quartz and calcite, the measured homogenization temperatures can be divided into five ranges: 230 to 320, 156 to 233, 138 to 213, 118 to 185, and 96 to 154 °C; Fig. 13), corresponding respectively to the formation temperatures of quartz and calcite during mineralization stages I, II, III, IV, and V, respectively.

Except for the ore-barren quartz stage during which the temperatures were relatively high (220 to 320 °C), the homogenization temperatures of fluid inclusions in quartz and calcite associated with the main and late stages of metallogenesis are all lower than 223 °C, and the ore-forming temperatures essentially the range between 120 and 210 °C. Ye and Ye (1998) and Ye et al. (1999a) drew similar conclusions in their studies in that the deposit appeared to have been formed under epithermal conditions.

6.3. Isotope geochemistry

6.3.1. Sulfur isotopic compositions

Sulfur isotopic analyses were carried out on 41 sulfide samples from different stages of mineralization (Table 3): 3 pyrite and 1 arsenopyrite samples from stage I; 15 pyrite and 3 pyrrhotite samples from stage II; 2 arsenopyrite, 11 pyrite and 1 stibnite samples from stage III; and 5 jamesonite/stibnite samples from stage IV. Results show that the $\delta^{34}S$ values vary from −3.0 to + 2.61‰, averaging 0.05‰ (Fig. 14). The average measured $\delta^{34}S$ values of arsenopyrite, pyrite, pyrrhotite and jamesonite are 0.73, 0.39, −0.05 and −1.26‰, respectively, following, as expected, the fractionation order of $\delta^{34}S_{arsenopyrite} > \delta^{34}S_{pyrite} > \delta^{34}S_{pyrrhotite} > \delta^{34}S_{jamesonite}$. The sulfides from the different stage have broadly similar $\delta^{34}S$ values with only a narrow range of variation (Fig. 14).

6.3.2. Lead isotopic compositions

As galena is not abundant and is only finely dispersed in the ore, it is very hard to select monomineralic fractions. The authors therefore carried out Pb isotopic

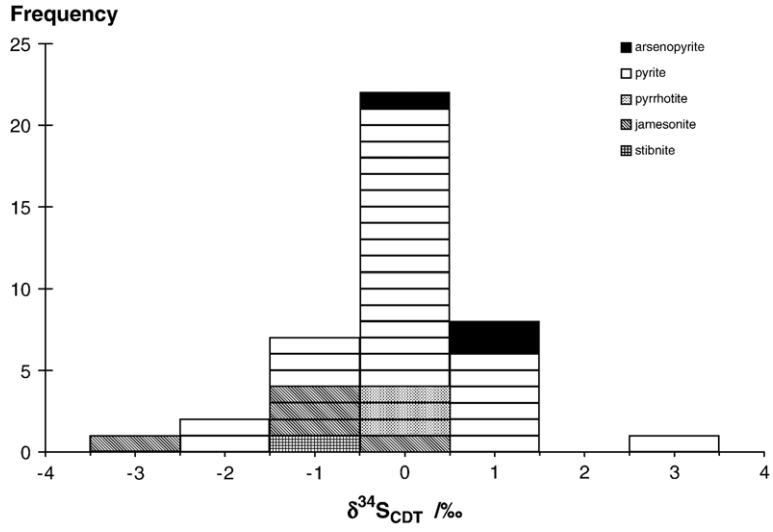

Fig. 14. Sulfur isotope distributions in the Sawaya'erdun gold deposit.

compositional analyses on other sulfides (4 arsenopyrites, 20 pyrites, 3 pyrrhotites, 1 stibnite and 3 jamesonites), siderite and quartz in the ore and ore-host rocks.

Ore lead isotopic compositions are rather uniform (Table 4), as evidenced by the Pb isotopic ratios: $^{206}Pb/^{204}Pb = 17.965$ to 18.348; $^{207}Pb/^{204}Pb = 15.539$ to 15.749; and $^{208}Pb/^{204}Pb = 38.062$ to 39.029. Pb isotope compositions are generally consistent with those of carbonaceous slate and sandy slate, indicating that they have a common source of lead. However, the single-stage Pb modal ages of ores (181.95 to 472.48 Ma) vary greatly, reflecting the multi-stage evolutionary character of the lead (Zheng et al., 2001, 2002; Liu et al., 2002a).

6.3.3. Carbon and oxygen isotopic compositions

Siderite, quartz, and calcite are the most important gangue minerals in the deposit. The results of C and O isotope analysis for siderite and calcite in ore and CO_2 in quartz and siderite inclusions are given in Table 5. As can be seen from the table, $\delta^{13}C$ and $\delta^{18}O$ values of CO_2 in the fluid are highly variable from −10.50 to +4.98‰ (average on −1.84‰) and +4.4 to 24.2‰ (average on +14.95‰), respectively. As graphite and carbonate minerals are not seen to coexist in the deposit, the CO_2 contents of fluid inclusions are far higher than those of CO and CH_4, i.e., CO_2 is the dominant C-bearing constituent in the hydrothermal system. It can thus be assumed that $\delta^{13}C_{fluid} = \delta^{13}C_{CO2}$ (Ohmoto, 1972), and therefore, the $\delta^{13}C$ values of the fluid are around −1.84‰. The $\delta^{13}C$ values of CH_4 in quartz fluid inclusions vary from −27.7 to −23.9‰, with an average of −25.8‰.

6.3.4. Si isotopic compositions

Silicon isotope analysis was performed on 7 hydrothermal quartz and 6 whole rock samples, the latter including chert, siltstone, slate and diabase dyke. The $\delta^{30}Si$ values (Table 6) of hydrothermal quartz in the deposit, except for a single sample that has a relatively large positive $\delta^{30}Si$ value of +0.5‰, all lie within the range of −0.7 to −0.1‰. Such values are smaller than those (+0.1 ~ +1.9‰) of cherts and diabase dyke in the mine district but are similar to those of ore-hosting siltstones, fine-grained sandstones and carbonaceous slates (−0.5 to −0.2‰).

6.3.5. Hydrogen and oxygen isotopic compositions of fluid inclusions

A total of 25 quartz and siderite samples from different stage of mineralization were analyzed for $\delta^{18}O$ of the host quartz and siderite, and δD values of fluid from fluid inclusions. Results are shown in Table 5. The $\delta^{18}O$ values of fluids are calculated from the $\delta^{18}O$ of quartz and siderite based on the equations $1000\ln\alpha(\text{quartz–water}) = 3.38\times10^{6}T^{-2} - 2.90$ (Friedman and O'Neil, 1977) and $1000\ln\alpha$ (siderite–water) $= 2.88\times10^{6}T^{-2} - 2.70$ (O'Neil and Silberman, 1974) using filling temperatures of fluid inclusions in quartz (Th). The δD values of fluids were directly taken from the measurements of from fluid inclusions. The $\delta^{18}O$ and δD values of ore-forming fluids vary, respectively, from −11.6 to +6.3‰ and from −84 to −38‰ for different stage of mineralization.

Table 4
Pb isotopic compositions of the rocks and hydrothermal minerals from the gold deposit

No.	Sample no.	Mineral and rock	$^{206}Pb/^{204}Pb(2\sigma)$	$^{207}Pb/^{204}Pb\ (2\sigma)$	$^{208}Pb/^{204}Pb(2\sigma)$
1	S016-2	Arsenopyrite	18.116(10)	15.621(10)	38.464(10)
2	S042-2	Arsenopyrite	18.054(10)	15.559(10)	38.210(10)
3	SII-20-2	Arsenopyrite	17.965(6)	15.553(2)	38.164(5)
4	SII-41	Arsenopyrite	18.062(3)	15.584(3)	38.281(10)
5	S016-1	Pyrite	18.165(10)	15.639(10)	38.597(10)
6	S042-1	Pyrite	18.108(10)	15.638(10)	38.452(10)
7	s0-70-1	Pyrite	18.259(7)	15.749(8)	38.712(19)
8	s0-70-3	Pyrite	17.969(8)	15.59(11)	38.239(32)
9	SI-11	Pyrite	18.160(4)	15.582(3)	38.329(9)
10	SII-41	Pyrite	18.102(5)	15.644(6)	38.430(17)
11	SII-42	Pyrite	18.058(4)	15.626(4)	38.355(8)
12	SII97-3	Pyrite	18.016(2)	15.557(1)	38.165(3)
13	SIV97-1	Pyrite	18.088(2)	15.623(1)	38.364(9)
14	SIV97-2	Pyrite	18.088(2)	15.625(3)	38.385(10)
15	SIV97-23	Pyrite	18.101(3)	15.627(3)	38.414(7)
16	SIV97-30	Pyrite	18.348(3)	15.615(3)	39.029(10)
17	SIV97-6	Pyrite	18.101(2)	15.638(2)	38.431(4)
18	SIV97-22	Stibnite	18.005(4)	15.539(4)	38.100(8)
19	SIV97-1	Pyrrhotite	18.062(2)	15.592(3)	38.260(4)
20	SIV97-2	Pyrrhotite	18.096(1)	15.633(1)	38.399(3)
21	SIV97-23	Pyrrhotite	18.027(5)	15.573(2)	38.208(8)
22	SII-19-1	Jamesonite	18.081(1)	15.606(1)	38.312(4)
23	SII-19-2	Jamesonite	18.136(2)	15.685(2)	38.579(4)
24	SIV97-27	Jamesonite	18.016(2)	15.576(2)	38.173(16)
25	S039	Siderite	18.002(10)	15.603(10)	38.229(10)
26	S026	Quartz	18.299(10)	15.547(10)	38.062(10)
27	S020	Slate	18.382(10)	15.637(10)	38.752(10)
28	97sw-23	Pyrite	18.099(5)	15.486(16)	38.194(12)
29	98sw-33	Pyrite	18.201(12)	15.609(8)	38.581(14)
30	27kd-03	Pyrite	18.203	15.580	38.427
31	sk-01	Pyrite	18.123	15.609	38.442
32	tc24-q2	Pyrite	18.065	15.600	38.311
33	sg-23-1	Pyrite	18.176	15.570	38.522
34	sg-25	Pyrite	18.012	15.603	38.304
35	sg-24	Slate	18.159	15.597	38.228
36	sg-29	Slate	18.049	15.584	38.085
37	sw-11-1	Slate	18.144	15.563	38.260

Samples 1–27 were analyzed at the Isotope Analysis Center of the Yichang Institute of Geology and Mineral Resources, CAGS; Samples 28 and 29 were analyzed at the State Key Laboratory of Environmental Geochemistry, Institute of Geochemistry, CAS; data for the others (30–37) were published by Ye et al. (1999a). Data in the brackets are analytical errors (2σ).

Table 5
The carbon, oxygen and hydrogen isotopic compositions of siderite, quartz and their inclusions

No.	Sample no.	Mineral	Stages of mineralization	Fluid inclusions							
				$\delta^{13}C$ (PDB)	$\delta^{18}O$ (SMOW)	$\delta^{13}C_{CO_2}$ (PDB)	$\delta^{18}O_{CO_2}$ (SMOW)	$\delta^{13}C_{CH_4}$ (PDB)	$\delta^{18}O_{H2O}$ [a] (SMOW)	δD [b] (SMOW)	Th [c] (°C)
1	S010	Quartz	Stage I			−5.8	24.2				250
2	98j-01	Quartz	Stage I			−0.3		−27.7		−51	272
3	98t-12	Quartz	Stage I			−1.4		−23.7		−56	252
4	98t-16	Quartz	Stage I			−8.1		−25.6		−80	198
5	98t-29	Quartz	Stage I			−0.4		−24.5		−80	205
6	S016	Quartz	Stage I			−5.2	14.5		5.7	−72	275
7	S026	Quartz	Stage II			−2.4	16.7		2.2	−59	190
8	97sw-51	Quartz	Stage II		19.0				6.3	−52	192
9	97sw-52	Quartz	Stage II		17.4				5.9	−54	211
10	97sw-62	Quartz	Stage II		19.3				4.7	−61	166
11	97sw-82	Quartz	Stage II		17.1				5.2	−56	205
12	98sm-7	Quartz	Stage II			−3.5		−27.4		−55	191
13	97sw-2	Quartz	Stage III			5.0			−3.0	−43	149
14	97sw-12	Quartz	Stage III			−0.3			−1.2	−65	183
15	97sw-14	Quartz	Stage III			0.1			2.4	−38	169
16	97sw-16	Quartz	Stage III			0.9			0.0	−50	175
17	97sw-64	Quartz	Stage III		18.8				3.1	−59	153
18	97sw-66	Quartz	Stage III		17.6				5.1	−52	195
19	97sw-81	Quartz	Stage III		20.5				6.2	−65	170
20	97sw-1	Quartz	Stage IV			0.0			−1.6	−50	124
21	97sw-21	Quartz	Stage IV			−0.7			−2.0	−54	145
22	97sw-31	Quartz	Stage IV			0.9			−1.5	−69 (−64) [d]	161
23	97sw-32	Quartz	Stage IV			4.8			−1.8	−47	153
24	97sw-35	Quartz	Stage IV			4.0			−3.3(−3.6)[d]	−68	135
25	97sw-21	Siderite	Stage V	−5.3 (−5.4)[d]	26.0 (25.9)[d]	−3.6			2.9	−54	138
26	S046	Siderite	Stage V			−10.5	4.4		−11.6	−62	125
27	S018	Siderite	Stage V	−3.4	18.6						111
28	97sw-32	Calcite	Stage V	−5.2	18.0						123
29	IV-1-9	Quartz	Stage			−8.7			−6.9	−65	
30	TC-01	Quartz	Stage			−5.3			−6.4	−82	
31	Tc-02	Quartz	Stage						−6.5	−84	
32	sg-04	Quartz	Stage			−4.5			−7.7	−67	

Samples Nos. 1–28 were analyzed at the Isotope Analysis Center of the Yichang Institute of Geology and Mineral Resources, CAGS; data for the others (29–32) were published by Ye et al. (1999a).

[a] Calculated based on the equations $1000\ln\alpha_{quartz-water} = 3.38\times10^6T^{-2} - 2.90$ (Friedman and O'Neil, 1977) and $1000\ln\alpha_{siderite-water} = 2.88\times10^6T^{-2} - 2.70$ (O'Neil and Silberman, 1974) using filling temperatures of fluid inclusions in quartz (Th).

[b] Water from fluid inclusions in quartz, siderite, and calcite.

[c] Filling temperatures of fluid inclusions (Zheng et al., 1996; Long et al., 1998).

[d] Data in the brackets are repeat analyses.

6.4. Age of mineralization

6.4.1. $^{40}Ar/^{39}Ar$ isotopic age

Following irradiation, quartz chips (1 to 3 mm in size, total 60 to 90 mg), having been pre-selected for purity under a binocular microscope, were analyzed by two bulk extraction techniques, crushing in vacuum and stepped heating. Gas released from quartz samples heated in a tightly closed container was analyzed on a mass spectrometer for Ar isotopes. The $^{40}Ar/^{39}Ar$ age data are listed in Table 7 and results of pre-treatment are shown in Fig. 15. As can be seen from the figure and table, the $^{40}Ar/^{39}Ar$ age spectrum for quartz samples from the Sawaya'erdun gold deposit is saddle-shaped, which show that the lowest apparent ages range from 206.09±6.00 to 208.07±1.22 Ma and the plateau ages in the age spectrum from 208.33±0.55 to 210.59±0.99 Ma.

6.4.2. Rb–Sr isotopic ages on fluid inclusions in quartz

Ye et al. (1999a) and the authors of the present paper conducted Rb–Sr isotopic analysis on 19 quartz fluid inclusions from auriferous quartz veins in the

Table 6
δ^{30}Si values (‰) of the rock and ore-forming quartz veins from the Sawaya'erdun gold deposit

No.	Sample no.	Mineral and rock	$\delta^{30}Si_{-NBS-28}$
1	97A74	Grayish green chert	1.9
2	98s-20	Black chert	0.4
3	97s-23	Diabase	0.1
4	97A-31	Silty sandstone	−0.5
5	97A59	Siltstone	−0.2
6	97A-61	Carbonaceous slate	−0.3
7	97sw-1	Quartz	−0.1
8	97sw-2	Quartz	−0.4
9	97sw-14	Quartz	0.5
10	97sw-16	Quartz	−0.1
11	97sw-32	Quartz	−0.1
12	97sw-21	Quartz	−0.5
13	97s-33	Gold ore	−0.7

Samples were analyzed at the Stable Isotope Laboratory, Institute of Mineral Resources, CAGS.

Sawaya'erdun deposit; results are listed in Table 8. Because all quartz samples analyzed were products of the main metallogenic stage in ore zone IV and the analyses were carried out in the same laboratory as those of Ye et al. (1999a), we report on the further treatment of both sets of data in an attempt to acquire reliable chronological data.

We conducted fitting treatment of all Rb–Sr isotopic ratios in 19 quartz fluid inclusions using a least-squares method. The slope of the acquired Rb–Sr isochron line is equal to 0.004092±0.000718, the Rb–Sr isochron age, t, is 288±50 Ma, and the initial $(^{87}Sr/^{86}Sr)_0$ ratio is 0.714918±0.000644. The Rb–Sr isochron of the 19 quartz fluid inclusions possesses good linearity (Fig. 16; r=0.9459), demonstrating that Sr isotopic homogenization occurred during metallogenesis.

7. Discussion

7.1. Implication of REE distribution patterns

The samples of ores and hydrothermal minerals can be divided into three groups in accordance with their REE distribution patterns. The REE distribution patterns of the first group (Fig. 12B) may indicate that sedimentary rocks in this region provided some ore-forming material. The features of the second group (Fig. 12C) reflect involvement of lower crust or mantle material in gold mineralization. The features of the third group (Fig. 12D), however, indicate that LREE/HREE fractionation occurred during evolution of ore-forming fluids, and that HREE were significantly enriched during the late stage of mineralization.

7.2. Genetic implications of stable and radiogenic isotopes

7.2.1. Sulfur isotopes

Sulfides from the different stage all show very narrow ranges of δ^{34}S values. Ore deposits with such sulfur isotopic characteristics are believed to have formed in a semi-closed geological environment, or in an environment in which the sulfur was derived from intermediate-basic volcanic rocks in the underlying strata, or, alternatively, sulfur was supplied from a deep source (Chen, 1994; Liu et al., 2000b,c, 2001). Considering the existence of a number of thick volcanic layers in strata of various ages underlying the Silurian–Devonian series in the southwestern Tianshan Mountains, underground aqueous solutions could extract metals, sulfur and other components from the volcanic layers when circulating through them. So these aqueous solutions would be important suppliers of sulfur and other components. The data, with δ^{34}S values for different minerals following the anticipated order, indicate consistency with sulfur isotope equilibrium fractionation.

According to Ohmoto (1972), S-bearing mineral assemblages are formed from hydrothermal solutions with certain ΣS isotopic composition and its δ^{34}S values vary with T, pH, fO_2, etc. Particularly when log fO_2 is relatively high (>−42), δ^{34}S values are very sensitive to the variation in fO_2 and pH. Slight variations in fO_2 and pH will lead to a great variation in δ^{34}S (Liu et al., 2000b). With the evolution of hydrothermal activity, if the early minerals were enriched in ^{34}S, the residual hydrothermal solutions would be relatively enriched in ^{32}S. Therefore, minerals crystallized from the residual solutions would also be low in ^{34}S. Under medium fO_2 conditions, the $\delta^{34}S_{\Sigma s}$ values of fluid producing the pyrite-chalcopyrite-sphalerite assemblage are close to those of pyrrhotite but smaller than those of pyrite, i.e., that $\delta^{34}S_{\Sigma s} < \delta^{34}S_{pyrite}$ (0.39‰), but approximately the same as $\delta^{34}S_{pyrrhotite}$ (−0.05‰).

7.2.2. Lead isotopes

To characterize the tectonic environment of the source region of ore lead, the Pb isotope data from various ore deposits can be plotted against the different evolutionary curves relative to Pb plumbotectonic models. As can be seen from the $^{207}Pb/^{204}Pb$–$^{206}Pb/^{204}Pb$ diagram (Fig. 17A), the data of hydrothermal sulfides and quartz from the deposit mainly fall near the orogenic Pb evolutionary curve, and between the orogenic and upper crust Pb evolutionary curves, partly showing a transitional trend to the mantle source. In the $^{208}Pb/^{204}Pb$–$^{206}Pb/^{204}Pb$ diagram (Fig. 17B), the data for ore lead are

Table 7
$^{40}Ar/^{39}Ar$ fast neutron activation analysis data of quartz from the Sawaya'erdun gold deposit

Incremental heating	Heating temperature (°C)	$(^{40}Ar/^{39}Ar)_m$	$(^{36}Ar/^{39}Ar)_m$	$(^{37}Ar/^{39}Ar)_m$	$(^{38}Ar/^{39}Ar)_m$	$(^{39}Ar)_k 10^{-12}$mol	$^{39}Ar_k$%	$^{40}Ar/^{39}Ar_k$ (±1σ)	Appearance age (Ma) (±1σ)
Conditions for sample 97sw–16: weight 0.40 g, irradiation parameter J 0.01219, irradiation time 55 h 47 mins., intermittent flux of neutrons 6.63×10^{12} n/cm^2.s, integrated flux of neutrons 1.32×10^{18} n/cm^2									
1	420	41.139	0.0728	0.1101	0.1835	0.37	3.24	19.72±1.01	388.61±24.86
2	550	27.674	0.0488	0.1142	0.1674	0.41	4.41	13.21±0.46	271.02±8.10
3	650	16.622	0.0216	0.1051	0.1270	0.86	7.59	10.25±0.16	212.36±2.33
4	730	13.947	0.0131	0.1310	0.1719	1.32	11.7	10.07±0.12	208.86±1.63
5	800	12.061	0.0069	0.1061	0.1473	3.04	26.9	10.03±0.09	208.07±1.22
6	880	12.921	0.0081	0.1575	0.2416	2.06	18.2	10.28±0.10	212.93±1.44
7	980	15.077	0.0161	0.2172	0.2692	1.51	13.3	10.33±0.14	214.00±1.95
8	1100	26.808	0.0468	0.5572	0.6596	0.54	4.82	13.10±0.43	267.34±7.55
9	1200	33.505	0.0593	0.6161	0.7371	0.45	3.98	16.14±0.67	324.09±14.04
10	1350	42.038	0.0764	0.6320	0.7325	0.36	3.22	19.63±1.06	387.08±25.90
11	1550	52.344	0.1016	0.5355	0.8437	0.21	2.62	22.54±1.64	438.04±44.79
Conditions for sample 97sw–31: weight 0.02596 g, irradiation parameter J 0.010863, irradiation time 62 h, intermittent flux of neutrons 5×10^{12} n/cm^2.s, integrated flux of neutrons 1.08×10^{18} n/cm^2									
1	380	63.888	0.16161	1.7172	0.61111	0.4588	5.35	16.50±0.05	297.57±14.26
2	460	41.016	0.10169	1.1837	0.46779	0.6838	7.98	11.20±0.04	207.18±7.27
3	540	27.573	0.05588	1.0946	0.26029	1.576	18.4	11.21±0.02	207.39±4.40
4	620	30.727	0.0663	0.63491	0.30363	1.275	14.8	11.24±0.02	207.98±4.98
5	700	32.261	0.0714	0.89707	0.35238	0.9737	11.3	11.31±0.02	209.21±5.65
6	820	35.833	0.0833	1.1997	0.43055	0.8345	9.74	11.41±0.03	210.97±6.78
7	950	44.5	0.10714	1.444	0.47142	0.6489	7.58	13.10±0.04	240.16±8.53
8	1100	45.312	0.10625	1.2348	0.47812	0.7417	8.66	14.16±0.04	258.22±9.26
9	1300	43.888	0.0972	1.1486	0.45277	0.8345	9.74	15.38±0.03	278.89±9.46
10	1500	63.695	0.15217	2.0776	0.71739	0.5328	6.22	19.13±0.06	340.73±18.23
Conditions for sample 97sw–32: weight 0.2669 g, irradiation parameter J 0.010863, irradiation time 62 h, intermittent flux of neutrons 5×10^{12} n/cm^2.s, integrated flux of neutrons 1.08×10^{18} n/cm^2									
1	380	64.926	0.16097	1.9541	0.64878	0.4749	5.54	17.76±0.05	318.26±15.97
2	460	29.217	0.0608	0.95594	0.3113	1.333	15.5	11.38±0.02	210.33±5.11
3	540	29.09	0.0606	0.93164	0.30151	1.53	17.8	11.33±0.02	209.43±4.96
4	620	31.25	0.0687	1.3974	0.38749	1.112	12.9	11.14±0.03	206.09±6.00
5	700	35.694	0.0833	1.6303	0.53888	0.8342	9.74	11.32±0.04	209.33±8.19
6	820	41.438	0.10273	1.9781	0.64383	0.6765	7.9	11.39±0.05	210.59±9.79
7	950	47.148	0.11787	2.2316	0.6806	0.6092	7.11	12.68±0.05	232.86±11.47
8	1100	45.909	0.10606	2.0044	0.65151	0.7645	8.92	14.89±0.05	270.64±12.65
9	1300	57.959	0.14285	2.7759	0.83265	0.5673	6.62	16.20±0.06	292.57±17.54
10	1500	53.754	0.1228	2.0594	0.6807	0.6602	7.71	17.82±0.05	319.39±15.71

Samples were analyzed at the Isotope Laboratory, Institute of Geology and Geophysics, CAS.

all concentrated near the orogenic Pb evolutionary curve, partly showing a transitional trend to the lower crust. This demonstrates that ore lead is derived predominantly from the crust, although the involvement of mantle-sourced lead cannot be ruled out (Zheng et al., 2002).

7.2.3. Silica isotopes

Available studies have shown that variation of $\delta^{30}Si$ values is controlled by Si isotope dynamic fractionation. The first precipitated silica has the lowest $\delta^{30}Si$ value. With increasing proportion of precipitated silica, $\delta^{30}Si$ values will increase steadily to a large, positive value (Ding et al., 1994). Studies by Clayton (1986) also indicate that when SiO_2 is leached out of the rocks by hydrothermal solutions, Si isotope fractionation will not generally take place. However, when SiO_2 is precipitated from hydrothermal solutions, $\delta^{30}Si$ fractionation between precipitated SiO_2 and the residual SiO_2 in the hydrothermal solutions will occur, but to varying degrees. If temperatures of hydrothermal solutions are relatively high, SiO_2 will be rapidly and completely precipitated, and such Si isotope fractionation mentioned above would be negligible. In contrast, if temperatures are relatively low, SiO_2 will be precipitated slowly and incrementally,

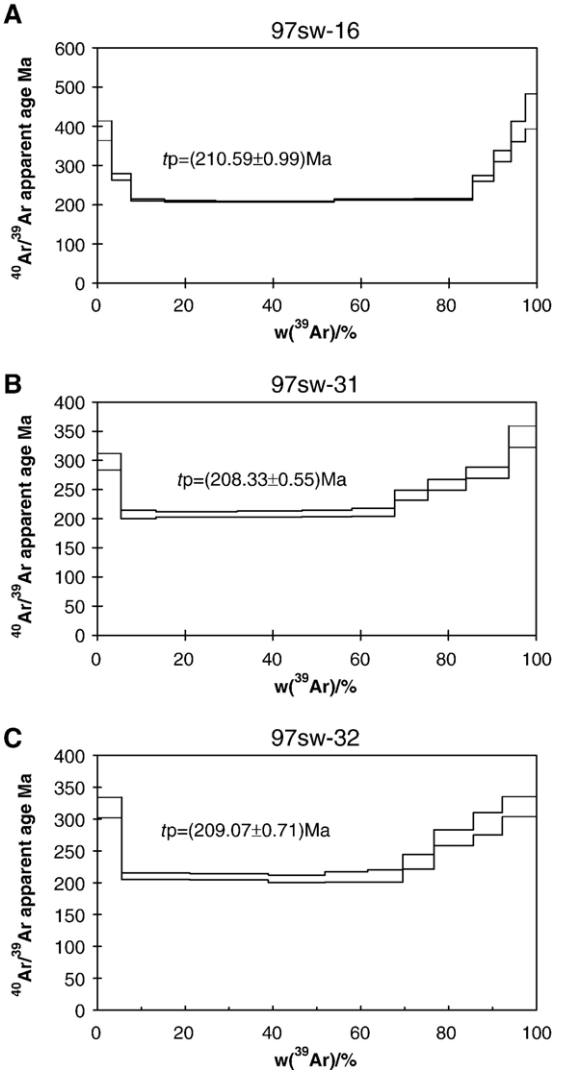

Fig. 15. The ^{40}Ar–^{39}Ar age spectrum of Au-bearing quartz from the Sawaya'erdun gold deposit. (A) $^{40}Ar/^{39}Ar$ age spectrum for sample 97sw-16 from ore zone no. IV. (B) $^{40}Ar/^{39}Ar$ age spectrum for sample 97sw-31 from ore zone no. IV. (C) $^{40}Ar/^{39}Ar$ age spectrum for sample 97sw-32 from ore zone no. IV.

and $\delta^{30}Si$ values of SiO_2 will be accordingly low. Formation temperatures of the Sawaya'erdun deposit are mainly in the range 110~220 °C, so the sedimentary ($\delta^{30}Si$= −0.5 to +1.9‰) and volcanic rocks ($\delta^{30}Si$=+0.1‰) in this region may have provided some silica for the ore-forming fluids (Liu et al., 2002a; Zheng et al., 2002).

7.2.4. Carbon and oxygen isotopes

The $\delta^{13}C$ values of CO_2 in the fluid are highly variable. By comparing the variation ranges of $\delta^{13}C$ values of CO_2 of various origins both in China and worldwide (Dai, 1988; Dai and Chen, 1993), it is inferred that CO_2 in the deposit may have two principal sources. One is derived from dissolution of carbonate rocks and the other is of endogenic inorganic origin. This feature is more precisely reflected on the $\delta^{13}C$–$\delta^{18}O$ plot (Fig. 18) in which the C and O isotopic values of CO_2 in crustal fluids from three principal sources (organic matter, marine carbonate rocks, and magma-mantle source) are shown. The variation trends of C and O isotopic compositions of CO_2 from the three sources, formed through five major geological processes, are marked by arrows (Liu and Liu, 1997; Mao et al., 2002; Liu et al., 2004b). The plotted data (Fig. 18) indicate that CO_2 might have been derived not only from dissolution of marine sedimentary carbonate rocks, but also from a magmatic (mantle) source. In fact, the $\delta^{13}C$ values of CO_2 in fluid inclusions are concentrated within two ranges: (1) −10.5 to −2.35‰ (mean −5.75‰), probably reflecting involvement of a deep-source fluid; and (2) −0.74 to +4.98‰ (mean +1.63‰), approximating average $\delta^{13}C$ values of marine carbonate rocks (+0.56±1.55‰; Keith and Weber, 1964).

The $\delta^{13}C$ values of CH_4 in quartz fluid inclusions (−27.7 to −23.9‰) are approximately the same as those of CH_4 from hot springs distributed along the Tengchong–Guohe fault zone in western Yunnan (ca. −20‰; Dai, 1988; Liu et al., 2001), the geothermal area in Yellowstone, U.S.A. (−28.4 to −10.4‰; Macdonald et al., 1983), hot water from Kamchatka, Russia (−32.6 to −21.4‰; Macdonald et al., 1983), and four geothermal areas in Engava, New Zealand (−29.5 to −24.4‰; Lyon and Hulston, 1984). They are also close to the variation range of $\delta^{13}C$ values (−30 to −20‰) pointed out by Faure (1986), but differ from those of CH_4 from the closed interstices and caves of magmatic rocks (−14.6 to −3.2‰; Zorikin et al., 1984) and from free gases in magmatic rocks (−19.3 to −11.8‰; Zorikin et al., 1984). The $\delta^{13}C$ values of carbonaceous material in the ore (−25.5 to −21.7‰; Zheng et al., 1996) are also approximate to those of fluid. All this indicates that CH_4 in ore-forming fluid would probably be derived chiefly from thermal decomposition of organic matter. Theoretically, ΔCO_2–CH_4 should be 48.9~26.3‰ (Friedman and O'Neil, 1977), bearing in mind carbon isotope fractionation between CO_2 and CH_4 in coexisting minerals at 100 to 280 °C, but measured ΔCO_2–CH_4 (17.5~27.4‰) is noticeably smaller. This indicates a possibility that CH_4 in the ore-forming fluid was derived from CO_2, or alternatively, from interaction between CO and H_2 (degassing of carbonate in sedimentary rocks and water/rock interactions between brines, carbonate and argillaceous rocks). We, therefore, believe that the carbon in the deposit was

Table 8
Results of Rb–Sr isotopic analyses for the Au-bearing quartz fluid inclusions from the Sawaya'erdun gold deposit

No.	Sample No.	Mineral	Rb/$_{\mu}$g.g^{-1}	Sr/$_{\mu}$g.g^{-1}	Rb/Sr	^{87}Rb/^{86}Sr	^{87}Sr/^{86}Sr (2ó)
1	97sw12	Quartz	0.1159	3.297	0.035153	0.1015	0.71582±0.00005
2	97sw14	Quartz	0.3301	2.291	0.144086	0.4157	0.71643±0.00007
3	97sw16	Quartz	0.2145	3.372	0.063612	0.1835	0.71543±0.00005
4	97sw31	Quartz	0.2088	3.339	0.062534	0.1804	0.71456±0.00005
5	97sw32	Quartz	0.0308	4.007	0.007679	0.0222	0.71374±0.00006
6	97sw12-1	Quartz	0.119	3.287	0.036203	0.1045	0.71581±0.00006
7	97sw31-1	Quartz	0.2038	3.394	0.060047	0.1732	0.71457±0.00001
8	97sw32-1	Quartz	0.0309	3.978	0.00776	0.0224	0.7137±0.00002
9	tc-01	Quartz	0.514	2.405	0.213721	0.617	0.71759±0.00001
10	tc-02	Quartz	0.341	2.072	0.164575	0.476	0.71569±0.00001
11	27kd-01	Quartz	0.14	1.822	0.076839	0.222	0.71734±0.00001
12	IV-Q1	Quartz	0.441	2.131	0.206945	0.605	0.71712±0.00012
13	IV-Q2	Quartz	1.825	1.533	1.190476	3.439	0.72885±0.00002
14	Q2	Quartz	0.468	1.963	0.238411	0.687	0.71879±0.00001
15	IV-I-02	Quartz	0.483	1.478	0.326793	0.943	0.71771±0.00003
16	IV-I-9	Quartz	1.037	4.467	0.232147	0.670	0.71777±0.00007
17	IV-I-11	Quartz	0.258	2.498	0.103283	0.298	0.71793±0.00001
18	IV-I-14	Quartz	0.232	1.626	0.142681	0.412	0.71873±0.00008
19	IV-I-07	Quartz	0.262	2.408	0.108804	0.314	0.71631±0.00017

Note: Serial Nos. 1–8 samples were analyzed at the Isotope Analysis Center of the Yichang Institute of Geology and Mineral Resources, CAGS; data for the others were published by Ye et al. (1999a).

partly derived from interactions between ore-forming fluid and carbonate strata, and partly from the decomposition of organic matter.

7.2.5. Hydrogen and oxygen isotopes

In order to explore the properties of ore-forming fluids, our data (Table 5) were projected onto a diagram of hydrogen and oxygen isotopic composition for various types of water (Fig. 19). It can be seen that the data for quartz and siderite samples all fall outside the areas of typical magmatic or metamorphic waters, indicating that the ore-forming fluids consisted largely of groundwaters (meteoric waters). Some samples plot relatively close to the meteoric water line; others lie at a greater distance from the line. This so-called "δ^{18}O shift" reflects a degree of O isotope exchange between meteoric water and rock (Zhang, 1989; Liu et al., 1998b, 2000b; Zheng et al., 2001, 2002).

7.3. Age of mineralization

7.3.1. $^{40}Ar/^{39}Ar$ isotopic age

The saddle-shaped ^{40}Ar/^{39}Ar age spectrum indicates that the analyzed samples contain excess ^{40}Ar (Harrison and McDougall, 1981; Zeitler and Gerald, 1986; Li et al., 1995; Wang and Qiu, 1999; Ying, 2002; Ying and Liu, 2002). Generally, the low- and high-temperature apparent ages of the saddle-shaped age spectrum are relatively high, because of the release of obvious excess ^{40}Ar of various kinds. Such excess ^{40}Ar includes low-temperature cation-type and high-temperature anion-type excess ^{40}Ar (Li et al., 1995), or because excess argon is dominantly hosted in fluid inclusions (because the fluid inclusions contain K and Cl) and in mineral lattices (Wang and Qiu, 1999). The low-temperature excess argon contained in fluid inclusions is usually released at 400 to 700 °C, contributing a relatively small proportion of the total. But the high-temperature excess ^{40}Ar is chiefly hosted in quartz and is usually released above 1000 °C. This portion of excess ^{40}Ar is relatively large (Sang et al., 1994; Ying, 2002). The apparent ages obtained at high- and low-temperature stages are both geochronologically

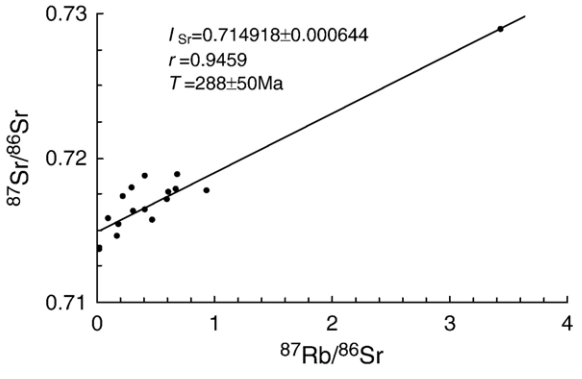

Fig. 16. The Rb–Sr isochronal ages of quartz fluid inclusions from the Sawaya'erdun gold deposits.

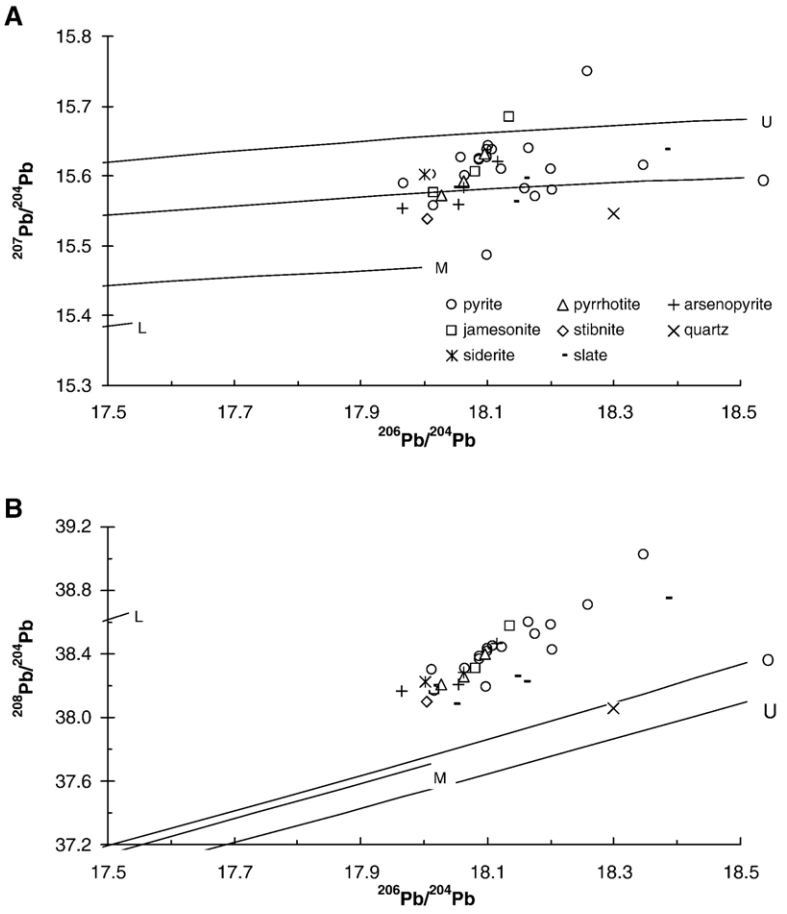

Fig. 17. Lead isotopic compositions of the Sawaya'erdun deposit (lead evolution model after Doe and Zartman, 1979; Zartman and Doe, 1981). M = upper mantle lead; O = orogenic belt lead; U = upper crustal lead; L = lower crustal lead.

meaningless (Sang et al., 1994; Liu et al., 2002b, 2003a, 2004a). In contrast, ages of geological significance can be acquired at the middle-temperature stage.

Since the ^{40}Ar–^{39}Ar age spectrum can be used to discriminate the excess ^{40}Ar in rock and minerals, the plateau age or lowest apparent age in this kind of age spectra is closer to the age of crystallization of the sample. The true ages of some samples can be acquired (Lanphere and Dalrymple, 1976; Zeitler and Gerald, 1986; Lanphere, 2000). Therefore, the lowest apparent age (206.09±6.00~208.07±1.22 Ma) or the plateau age in the age spectrum (208.33±0.55~210.59±0.99 Ma) of Au-bearing quartz veins can be regarded as the upper age limit of gold mineralization in the Sawaya'erdun gold deposits.

Included in the plateau ages are the age data acquired at five heating stages from 460 to 980 °C; the amount of released ^{39}Ar accounts for 62.22~77.69% of the total. The data points involved in the plateau age calculation can satisfy such pre-conditions that the sample was deposited at the same time from the cognate source under chemically closed condition (Folland, 1983; Zeitler and Gerald, 1986; Sang et al., 1994; Li et al., 1995). Therefore, isochron age calculations can be conducted. Our results (Fig. 20) show that the plateau age (208.33±0.55~210.59±0.99 Ma), the lowest apparent age (206.09±6.00~208.07±1.22 Ma) and the isochron age (206.05±2.38~208.25±3.39 Ma) are very close to each other. This tells us that the determined ages of the quartz samples may be both true and reliable and that the plateau age represents the time of formation of quartz, corresponding to Late Indosinian epoch. Furthermore, initial $(^{40}Ar/^{39}Ar)_i$ ratios (294.9±3.54~310±14.32 Ma) are close to atmospheric value (295.5±5), also indicating that the analyzed samples contain no excess ^{40}Ar or have suffered an obvious ^{39}Ar loss. This implies that excess ^{40}Ar have almost no impact on the analytical results and that our plateau ages are considered both precise and reliable. If the isochron intercept value significantly

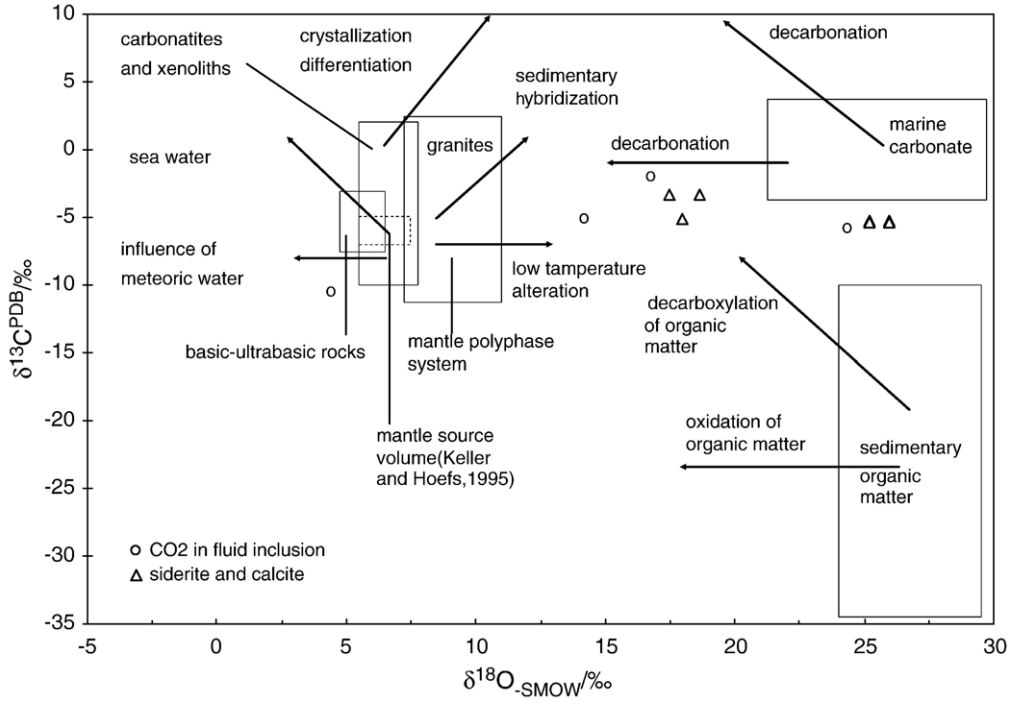

Fig. 18. $\delta^{18}O$ versus $\delta^{13}C$ diagram of siderite and fluid inclusions of quartz from the Sawaya'erdun deposits. For reference, the fields for typical marine carbonates (MC), sedimentary organic matter (Sed Org), igneous carbonate (CMX, carbonatite and mantle xenoliths; BUR, basic and ultrabasic rocks; G, granite) and mantle polyphase system (MM) are outlined. The arrows show typical isotopic trends resulting from carbonate dissolution (Dis Carb), decarbonation (Dec), decarboxylation of organic matter (Decbx), oxidation of organic matter (Oxid Org), crystallization differentiation (Crys Diff), influence of meteoric water (Influ MW), permeation of seawater (Perm SW), low tamperature alteration (LT alter) and sedimentary hybridization trend (Sed Hybr). See text for further description. Modified after Liu and Liu (1997), Liu et al. (2004b).

differs from 295.5, then the analytical data should be recalculated, in order to obtain the true age, using the intercept value for the composition of non-radiogenic Ar (Lanphere, 2000).

7.3.2. Rb–Sr isotopic ages on quartz fluid inclusions

We obtained a Rb–Sr isochron age of 288±50 Ma on quartz fluid inclusions from the deposit. However, it was attested by the method of $(^{87}Sr/^{86}Sr)_0-1/Sr$ (Wendt and Carl, 1991; Zheng, 1989) and isochron-fitted MSWD (mean squared weighted deviation; Vollmer, 1976; Yang et al., 2000) to be a mixed isochron age, and therefore carries no chronological significance. Table 8 also shows that $^{87}Rb/^{86}Sr$ is directly proportional to Rb/Sr and this feature can be explained by the isochron model or the mixing model (Qin, 1987). Considering the possibility that there was mixing during the hydrothermal event, the $(^{87}Sr/^{86}Sr)_0-1/Sr$ diagram was constructed (Fig. 21). The data for samples constituting the isochron are mostly not distributed around $I_{Sr}=0.714918\pm0.000647$, but instead tend to show a linear distribution. This may indicate that the samples constituting the isochron are, for the most part, the result of mixing. Although the isochron age obtained (T 288±50 Ma, and $I_{Sr}=0.71491\pm0.000647$) may indeed be indicative of a mixed isochron, we note with interest that this age is highly reminiscent of that given for the Muruntau deposit.

Our studies have shown that the formation of the Sawaya'erdun gold deposit is closely linked to mixing of

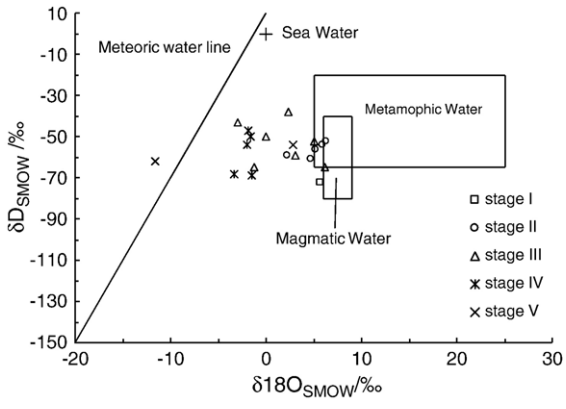

Fig. 19. $\delta^{18}O$ versus δD diagram of fluid inclusions of the Sawaya'erdun deposit (modified after Sheppard, 1986).

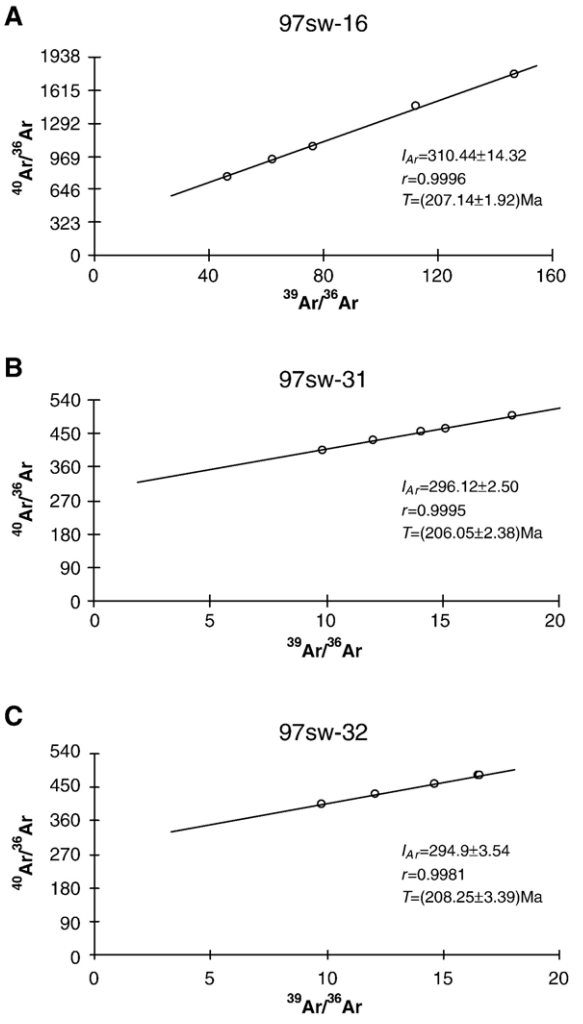

Fig. 20. The ^{40}Ar–^{39}Ar isochronal ages of Au-bearing quartz from the Sawaya'erdun deposits. (A) $^{40}Ar/^{39}Ar$ isochron diagram for sample 97sw-16. (B) $^{40}Ar/^{39}Ar$ isochron diagram for sample 97sw-31. (C) $^{40}Ar/^{39}Ar$ isochron diagram for sample 97sw-32.

infiltrating meteoric waters, which extracted ore-forming elements from the ore-hosting and underlying strata, with magmatic waters (Liu et al., 2002a). The diabase dyke, a product of magmatic activity in the region, is closely associated with gold metallogenesis, based on our geological and geochemical observations (Liu et al., 2002a). We therefore selected diabase dyke and host rock in this region as the two end-members. The initial condition of the diabase dyke end-member is $(^{87}Sr/^{86}Sr)_0$=0.707815 (obtained by substituting the K–Ar age, T=207 Ma of this sample into the Rb–Sr isotopic data), with Rb=49.36×10^{-6} and Sr=150.80×10^{-6}, which are the NAA average values of two diabase dyke samples. The initial condition of the host rock end-member is $(^{87}Rb/^{86}Sr)_0$=0.711509 (Liu et al., 1999), with Rb=84.76×10^{-6} and Sr=111.21×10^{-6}. This value is the average value of 29 host rock samples analyzed by NAA, including phyllite, siltstone and siliceous rock samples (Liu et al., 2002a).

According to the slope of the mixing isochron, $g=[((^{87}Sr/^{86}Sr)_A-(^{87}Sr/^{86}Sr)_B)/k[(Rb/Sr)_A-(Rb/Sr)_B]$, then k=2.90 (for calculation procedure see Faure, 1986; Qin, 1987; Zheng, 1989). The g value is figured to be 2.92925×10^{-3} and the calculated age, 206 Ma. This value represents closure time of the Rb–Sr isotopic system or the time of material mixing.

7.4. Genesis of the deposit

In the Sawaya'erdun region, both the Carboniferous ore-hosting clastic rock formation and the underlying Paleozoic strata are enriched in Au, Sb, and Hg (Ye et al., 1998, 1999b; Zheng et al., 2001). This created one favorable precondition for the formation of the deposit. Since Paleozoic times, the southwestern Chinese Tianshan region has experienced multiple episodes of tectonism, resulting in complex tectonic deformation and fragmentation of rocks (Zheng et al., 1996, 2001). The locations, where the original stress energy was large, have been converted to a depressurized dilatant zone, providing an important locus for late hydrothermal activity and ore formation.

Late hydrothermal metallogenesis in the region is closely associated with infiltration of meteoric water, so understanding of the heat source is a key to understand the forming mechanism of the deposit. It is commonly accepted that gold metallogenesis in the southwestern Tainshan region mainly occurred during the Late Carboniferous–Permian (Goldfarb et al., 2001; Mao et al., 2004). Since the Mesozoic, tectonomagmatic

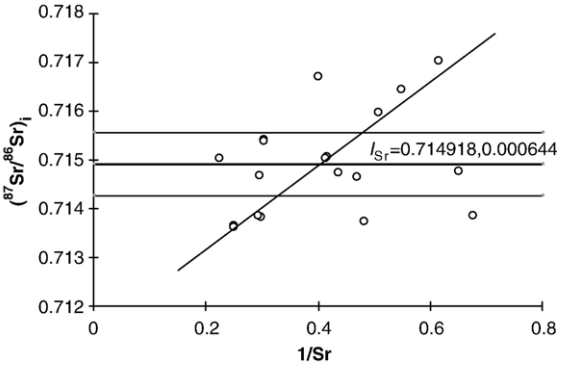

Fig. 21. $(^{87}Sr/^{86}Sr)_i$ versus 1/Sr diagram of quartz fluid inclusions from the Sawaya'erdun deposit.

activity in this region was only weak (Wu et al., 1998; Yang et al., 1999). Although there is no extensive exposure of intrusive rocks in the studied region, some diorite and diabase dykes have been found in the Carboniferous and Permian strata (Zheng et al., 2001; Liu et al., 2002a,b). This suggests that tectonomagmatic activity was also intense in this region during the post-Permian period. Available data show that Late Indosinian tectonomagmatic activity was not only intense but also accompanied by formation of base- and precious metal deposits in the southwestern Tianshan Mountains (Liu et al., 2002b). Therefore, the tectonomagmatic activities could not only provide some ore-forming components, including Au and Sb for the Sawaya'erdun gold deposit, but more importantly they provided a heat source to drive the hydrothermal system, leading to intensification of paleogeothermal activities during the Late Indosinian. The mineralization age provides strong evidence for formation of the Sawaya'erdun gold deposit (and other gold deposits in southwestern Chinese Tianshan Mountains) in the Late Indosinian. This reflects that a certain indispensable key factor leads to gold metallogeny and constrains deposit formation in an integrated manner during the Late Indosinian in the southwestern Chinese Tianshan Mountains.

Meteoric waters infiltrated downwards through fractures, extracting ore-forming elements from Au-bearing strata, forming mineralizing hydrothermal solutions. Density tends to decrease with rise in temperature. When these solutions reached a certain critical depth, they would return upwards into a favorable depressurized space, whereas the change of physico-chemical conditions (temperature, pressure, acidity-alkalinity and redox potential) would increase considerable concentrations of ore-forming materials, such as gold and base metals in the residual solutions after the crystallization of quartz. Sulfides and native gold would crystallize from the saturated solutions to form the economic orebodies.

8. Concluding remarks and comparison with Muruntau

The Sawaya'erdun gold deposit is the first case of a large, low-grade orogenic gold deposit in the Chinese portion of the Tianshan Mountains. In some ways, it can be compared with the Muruntau gold deposit in Uzbekistan with respect to geological setting, host lithology, mineralization style, mineral assemblages, geochemical association, metallogenic processes involved — and possibly also age.

The common features shared by the Sawaya'erdun and Muruntau are as follows.

(1) The regional geotectonic setting of the Sawaya'erdun deposit is consistent with that of the Muruntau gold deposit in adjacent Uzbekistan (Kotov and Poritskaya, 1993; Drew et al., 1996). Both deposits are controlled by the Turkestan suture zone (Cai et al., 1993; Mao et al., 2004).

(2) Lithological characteristics of the ore-hosting strata are a suite of typical turbidities (Zheng et al., 1996, 2001) in both cases, although the age of the ore-hosting strata is Late Carboniferous for Sawaya'erdun (Liu et al., 1999) and is either Ordovician–Silurian (according to Mukhin et al., 1988; Uspenskiy and Aleshin, 1993; Loshchinin, 1996; Kempe et al., 2001), Cambrian–Ordovician (according to Mukhin et al., 1988; Cai et al., 1993; Tan, 1993), or Precambrian–Lower Paleozoic (according to Drew et al., 1996; Skryabin et al., 1997) for Muruntau.

(3) Mineralization is controlled by fracture zones, and orebodies are composed of ore-bearing quartz veins or quartz–siderite veinlets or network veins. The ore minerals and the ore types in the veins are comparable.

(4) There exist a large number of base metal sulfides and bismuth minerals associated with gold minerals in both deposits. Mineral assemblages differ from those of Carlin-type gold deposits, which are characterized by a low-temperature mineral assemblage of arsenopyrite-(As) pyrite-realgar-orpiment-cinnabar (Arehart, 1996; Liu et al., 2000d, e, 2003b).

(5) The extensive Au–As–Sb–Hg–Ag–Bi geochemical anomalies over a very large area in the Sawaya'erdun field, with perfect element association and distinct zonation (Liu et al., 1998a) are also consistent with those in the Muruntau deposit (Skryabin et al., 1997).

(6) The Muruntau deposit is characterized by the presence of visible gold (generally within the range 0.001 to 1 mm), which is present as micro-fine enclaves scattered in quartz and sulfides. The gold also occurs as micro-fine veinlets (Cai et al., 1993; Tan, 1993). Abundant microscopic gold and gold veinlets were also recognized in the Sawaya'erdun deposit (Zheng et al., 1996; Liu et al., 2000a; Zheng et al., 2001). Recovered gold is distributed in the fragmented parts of quartz and arsenopyrite or pyrite or at the rims of the mineral grains.

(7) The Sawaya'erdun deposit is generally similar to the Muruntau deposit with respect to its multi-episode and multi-stage metallogenesis.

The Sawaya'erdun gold deposit also possesses some unique features.

(1) The ore-forming temperature is low. As stated above, with the exception of the ore-barren quartz stage at which the temperature was relatively high (220 to 320 °C), homogenization temperatures of quartz fluid inclusions associated with metallogenesis are all below 223 °C, mostly within the range 120 to 210 °C. However, with the exception of the fourth metallogenic stage at Muruntau, during which the temperature was relatively low (Zairi and Kurbanov, 1992), the average temperatures for the other three metallogenic stages all exceed 220 °C (generally in the range of 220 to 350 °C, even up to as much as 500 °C), significantly higher than any temperature estimate for Sawaya'erdun.
(2) The geochemical signatures are somewhat different. Although the Sawaya'erdun and Muruntau gold deposits are both characterized by high Ag anomalies, the silver mineralogy appears to be substantially different. Selenides and tellurides have been widely found in Muruntau (e.g., Drew et al., 1996), but in the Sawaya'erdun gold deposit no selenide or telluride mineral has yet been found. In addition, no high W anomalies have been found at Sawaya'erdun, yet Sb is much more abundant with Sb lodes defined. As for gold minerals, Muruntau deposit is dominated by native gold of high fineness (890 to 910; Cai et al., 1993; Liu et al., 1998a), whereas the Sawaya'erdun deposit is dominated by electrum with fineness of only 700 to 800 (Zheng et al., 1996; Liu et al., 2000a; Zheng et al., 2001). Formation of electrum is controlled by a number of dynamic factors such as element migration style, the extent of opening or closeness of the system and the precipitation mechanism of electrum itself (Wilkinson et al., 1999). Generally speaking, electrum is formed under low temperature conditions (e.g., Shelton et al., 1990), but can also be formed under high temperature conditions (Hagemann et al., 1998).

There is still uncertainty about whether formation of the Sawaya'erdun and Muruntau gold deposits was synchronous. Previous K–Ar and Rb–Sr dating of hydrothermal alteration and sulfide–quartz veins yielded four-phase ages from 272.6, 256.2, 230.2, and 219.4 Ma for the Muruntau gold deposit (Kotov and Poritskaya, 1992; Marakushev and Khokhlov, 1992). Kostitsyn (1993, 1996) obtained also Rb–Sr isochrons of density separates from auriferous quartz vein samples (include quartz-tourmaline vein, quartz-arsenopyrite veinlet and Ag–Au quartz-adularia veins) in the Muruntau of 257±13, 230±3.5, and 219±4.2 Ma. Recently, Wilde et al. (2001) obtained ^{39}Ar–^{40}Ar analytical results of stockpiled ore samples in the Muruntau deposit, which provided evidence of two sericite-forming events at about 245 and 220 Ma. Kempe et al. (2001) obtained Sm–Nd isochron of scheelite from steeply dipping veins in the Muruntau of 279±18 Ma, which is interpreted to date high-grade ore formation in the deposit. The span of ages for Muruntau is thus from 219 to 279 Ma (Kotov and Poritskaya, 1992; Marakushev and Khokhlov, 1992; Kostitsyn, 1993, 1996; Kempe et al., 2001; Wilde et al., 2001). The formation age of the Sawaya'erdun deposit is younger — if we exclude the Rb–Sr isochron age of 288±50 Ma discussed in Section 7.3.2 above. ^{39}Ar–^{40}Ar plateau and isochron ages of auriferous quartz samples range from 206 to 213 Ma, and Rb–Sr ages of quartz fluid inclusions give 206 Ma. Such ages are consistent with the ages for the Dashankou gold deposit (207.16±0.85~212.59±0.68 Ma; Liu et al., 2004a), and the Bulong gold deposit (212.18±0.83 Ma; Liu et al., 2004b), but is nevertheless consistent with the age of the fourth-phase age given for Muruntau (219.4±4.2 Ma; Kotov and Poritskaya, 1992; Marakushev and Khokhlov, 1992). It also agrees closely with the third of the three Rb–Sr ages (219±4.2 Ma) given by Kostitsyn (1993, 1996) or one of the two ^{39}Ar–^{40}Ar ages (220 Ma) of Wilde et al. (2001) from Muruntau. Both isotopic systems apparently record a succession of hydrothermal events.

Acknowledgements

Funding for this project was jointly granted by the 111 project (Grant No. B07011), by the National Natural Science Foundation of China (Grant No. 40073019, 40234051, and 40434011) and by the State No. 305 Program of Solving Key Problems in Science and Technology (No.95-04-03-01). Thanks are due to Chief Engineers Zhang Liangcheng, Liu Dequan and Wang Futong from the Xinjiang Bureau of Geology and Mineral Resources for their contribution to fieldwork and to Senior Engineers Luo Zhiling and Wang Jin from the No.2 Geological Party of Xinjiang Bureau of Geology and Mineral Resources for their great help. This manuscript has also benefited from the comments and critical reviews from *Ore Geology Reviews* referee Andy Wilde and Associate Editor Alexander Yakubchuk, who has also handled the manuscript.

References

Arehart, G.B., 1996. Characteristics and origin of sediment-hosted disseminated gold deposit: a review. Ore Geology Reviews 11, 383–403.

Cai, H., Zheng, Y., Li, F., 1993. Geological investigation of Muruntau gold deposit. Mineralogy and Geology 7, 408–413 (in Chinese with English abstract).

Chen, H., 1994. Ore Isotopic Geochemistry. Zhejiang University Press, Hangzhou, China. 340 pp. (in Chinese).

Chen, F., Li, H., 2003. Metallogenic Chronology of the Sawayaerdun Gold–Antimony Deposit in Xinjiang. Acta Geoscientia Sinica 24, 563–567 (in Chinese with English abstract).

Clayton, R.N., 1986. High temperature isotope effects in the early solar system. Stable isotopes in high temperature geological processes. In: Valley, J.W., Taylor Jr., O'Neil, J.R. (Eds.), Reviews in Mineralogy, vol. 16, pp. 129–139.

Clayton, R.N., Mayeda, T.K., 1963. The use of bromine pentafluoride in the extraction of oxygen from oxides and silicates for isotopic analysis. Geochimica et Cosmochimica Acta 27, 43–52.

Cliff, R.A., Janes, G., Choi, W.C., Lee, T.J., 1985. Strontium isotopic equilibration during metamorphism of tillites from Ogcheon belt, South Korea. Contributions to Mineralogy and Petrology 90, 346–352.

Coleman, M.L., Sheppard, T.J., Durham, J.J., Rouse, J.E., Moore, G.R., 1982. Reduction of water with zinc for hydrogen isotope analysis. Analytical Chemistry 54, 993–995.

Dai, J., 1988. Carbon isotopic composition characteristics and origin of natural gases at Liuhuangtang, Tengchong County, Yunnan Province. Chinese Science Bulletin 33, 1168–1170 (in Chinese).

Dai, J., Chen, Y., 1993. Carbon isotopic characteristics of alkane fraction in biogenic gases in China and their discriminating indicators. Science in China. Series B, Chemistry, Life Sciences & Earth Sciences 23, 303–305 (in Chinese).

Ding, T., Jiang, S., Wan, D., Li, Y., Li, J., Song, H., Liu, Z., Yao, X., 1994. Silicon Isotope Geochemistry. Geology Press, Beijing. 102 pp. (in Chinese).

Dodson, M.H., 1976. Kinetic processes and thermal history of slowly cooling solids. Nature 259, 551.

Doe, B.R., Zartman, R.E., 1979. Plumbotectonics. In: Barnes, H. (Ed.), Geochemistry of Hydrothermal Ore Deposits. John Wiley and Sons, New York, pp. 22–66.

Drew, L.J., Berger, B.R., Kurbanov, N.K., 1996. Geology and structural evolution of the Muruntau gold deposit, Kyzylkum Desert, Uzbekistan. Ore Geology Reviews 11, 175–196.

Fang, W., Hu, R., Xie, G., Su, W., Qi, L., 2001. Diagenetic-metallogenic ages of pyritic cherts and their implications in Mojiang nickel-gold deposit in Yunnan Province, China. Chinese Science Bulletin 46, 1823–1827.

Faure, G., 1986. Principles of Isotope Geology, 2nd ed. John Wiley and Sons, New York. 589 pp.

Folland, K.A., 1983. $^{40}Ar/^{39}Ar$ incremental heating plateaus for biotite with excess argon. Isotope Geoscience 1, 3–21.

Friedman, I., O'Neil, J.R., 1977. Compilation of stable isotope fractionation factors of geochemical interest. Data Geochemistry, In: Fleischer, M. (Ed.), 6th ed. United States Geological Survey Professional Paper, Washington DC, vol. 440-KK. 111 pp.

Goldfarb, R.J., Groves, D.I., Gardoll, S., 2001. Orogenic gold and geologic time: a global synthesis. Ore Geology Reviews 18, 1–75.

Hagemann, S.G., Brown, P.E., Ridley, J., Stem, P., Fournelie, J., 1998. Ore petrology, chemistry and timing of electrum in the Archean Hypozonal lode gold deposit, Western Australia. Economic Geology 93, 271–291.

Harrison, T.M., McDougall, I., 1981. Excess ^{40}Ar in metamorphic rocks from Broken Hill, New South Wales: implications for $^{40}Ar/^{39}Ar$ age spectra and the thermal history of the region. Earth and Planetary Science Letters 55, 123–149.

Hollister, L.S., 1982. Metamorphic evidence for rapid (2 mm/yr) uplift of a portion of the central gneiss complex, Coast Mountains. Canadian Mineralogist 20, 319–332.

Humphrises, F.J., Cliff, R.A., 1982. Sm–Nd dating and cooling history of Scourian granulites, Sutherland. Nature 295, 515.

Jiang, B., 1989. Methodology and its limitation of Archean rock dating. Geochemica 18, 103–120 (in Chinese with English abstract).

Keith, M.L., Weber, J.N., 1964. Carbon and oxygen isotopic composition of selected limestone and fossils. Geochimica et Cosmochimica Acta 28, 1787–1816.

Kempe, U., Belyatsky, B.V., Krymsky, R.S., Kremenetsky, A.A., Ivanov, P.A., 2001. Sm–Nd and Sr isotope systematics of scheelite from the giant Au(–W) deposit Muruntau (Uzbekistan); implications for the age and sources of Au mineralization. Mineralium Deposita 36, 379–392.

Knauth, I.P., Epstein, S., 1976. Hydrogen and oxygen isotope ratios in nodular and bedded cherts. Geochimica et Cosmochimica Acta 40, 1095–1110.

Kostitsyn, Y.A., 1993. Rb–Sr isotope study of the Muruntau deposit: dating of ore veins by the isochron technique. Geokhimiya 31, 1308–1319 (in Russian).

Kostitsyn, Y.A., 1996. Rb–Sr isotope study on the Muruntau deposit: magmatism, metamorphism, and mineralisation. Geokhimiya 34, 1123–1138 (in Russian).

Kotov, N.V., Poritskaya, L.G., 1992. The Muruntau gold deposit: its geologic structure, metasomatic mineral associations and origin. International Geology Review 34, 77–87.

Kotov, N.V., Poritskaya, L.G., 1993. The Muruntau gold deposit. Mineralogy in the service of mankind, Programme and Abstracts. International Congress on Applied Mineralogy, 1993 Annual Meeting, Freemantle, Australia, pp. 190–193.

Lanphere, M.A., 2000. Comparison of conventional K–Ar and $^{40}Ar/^{39}Ar$ dating of young mafic volcanic rocks. Quaternary Research 53, 294–301.

Lanphere, M.A., Dalrymple, G.B., 1976. Identification of excess ^{40}Ar by the $^{40}Ar/^{39}Ar$ age spectrum technique. Earth and Planetary Science Letters 32, 141–148.

Laznicka, P., 1983. Giant ore deposit: a quantitative approach. Global Tectonics and Metallogeny 2, 41–63.

Laznicka, P., 1989. Derivation of giant ore deposits. 28th International Geological Congress, Washington DC, United States, vol. 2, pp. 2268–2269. Abstracts.

Li, X., 1996. A discussion on the model and isochron ages of Sm–Nd isotopic systematics: suitability and limitation. Scientia Geologica Sinica 31, 97–104 (in Chinese with English abstract).

Li, X., Luo, W., 1997. Geological character of Sawaya'erdun gold deposit in Xinjiang: the first one of Muruntau-type gold deposit in China. Acta Geologica Gansu 6, 62–66 (in Chinese with English abstract).

Li, H., Liu, J., Wei, L., 1993. Fluid Inclusion Chronology of Hydrothermal Ore Deposits and its Geological Reply. Geological Press, Beijing, pp. 22–41.

Li, Z., Dai, T., Qiu, H., 1995. The release of $^{40}Ar(^{40}Ar^{*}+{}^{40}Ar_{E})$ and ^{39}Ar in ^{40}Ar–^{39}Ar samples and its chronological significance. Chinese Journal of Geology 30, 40–45 (in Chinese with English abstract).

Liu, J., Liu, J., 1997. Basinal fluid genetic model of fine disseminated gold deposits in the Golden Triangle area between Yunnan, Guizhou and Guangxi. Acta Mineralogica Sinica 17, 448–456 (in Chinese with English abstract).

Liu, D., Tang, Y., Zhou, N., 1998a. The direction of search for minerals of the Muruntau-type gold deposits in Xinjiang. Gold Science & Technology 6, 18–22 (in Chinese with English abstract).

Liu, J., Zheng, M., Zhou, D., Liu, J., Zhou, Y., Gu, X., Zhang, B., Lin, L., 1998b. The components and evolution of the hydrogen and oxygen isotopes of ore-forming fluids from Laerma gold ore belt. Journal of Changchun University of Science and Technology 28, 93–98 (in Chinese with English abstract).

Liu, J., Zheng, M., Long, X., Gu, T., 1999. Reidentification of the ore-hosted strata age of the Sawaya'erdun gold deposit in Xinjiang, southwestern Tianshan. Chinese Science Bulletin 44, 1811–1814.

Liu, J., Zheng, M., Long, X., Zhang, S., Yin, H., Wang, J., 2000a. Identification of Sawaya'erdun Muruntau gold deposit in Xinjiang, southwestern Tianshan Mountains Mountains and its signification. Journal of Precious Metallic Geology 9, 129–132 (in Chinese with English abstract).

Liu, J., Li, C., Pan, J., Hu, R., Liu, X., Zhang, Q., 2000b. Isotopic geochemistry in the copper deposits from sandstone and shale in Lanping-Simao basin, western Yunnan. Mineral Deposits 19, 223–234 (in Chinese with English abstract).

Liu, J., Zheng, M., Liu, J., Zhou, D., 2000c. Sulfur isotopic composition and its geological significance of the Cambrian gold deposits in western Qinling, China. Journal of Changchun University of Science and Technology 30, 150–156 (in Chinese with English abstract).

Liu, J., Liu, J., Zheng, M., Liu, X., 2000d. The Au–Se paragenesis in Cambrian stratabound gold deposits, Western Qinling Mountains, China. International Geology Review 42, 1037–1045.

Liu, J., Zheng, M., Liu, J., Su, W., 2000e. Geochemistry of the Laerma and Qiongmo Au–Se deposits in the western Qinling Mountains, China. Ore Geology Reviews 17, 91–111.

Liu, J., Li, C., Zhang, Q., Pan, J., Liu, Y., Liu, X., Liu, S., Yang, W., 2001. Wood textures in Jinman copper deposits in western Yunnan. Science in China, Series D: Earth Sciences 44, 545–554.

Liu, J., Zheng, M., Long, X., Yin, H., Wang, J., Li, E., 2002a. Metallogenic characteristics of Sawaya'erdun gold deposit in Xinjiang. Acta Mineralogica Sinica 22, 53–62 (in Chinese with English abstract).

Liu, J., Zheng, M., Long, X., Li, E., Wang, J., Sang, H., Yin, H., 2002b. The metallogenetic age of Sawaya'erdun gold deposit in Xinjiang, southwestern Tianshan Mountains. Journal of Mineralogy and Petrology 22, 19–23 (in Chinese with English abstract).

Liu, J., Li, Z., Zhang, Q., Liu, Y., Li, C., He, M., Sang, H., 2003a. The ^{40}Ar–^{39}Ar fast-neutron activation age of quartz from Jinman copper deposit, western Yunnan. Chinese Journal of Geology 38, 529–531 (in Chinese with English abstract).

Liu, J., Zheng, M., Liu, J., Gu, X., Zhou, Y., Feng, C., 2003b. Mechanical transport of metallogenic materials in hydrothermal solutions: Evidence from the microspherules in micro-disseminated gold deposits, northwestern Sichuan, China. Ore Geology Reviews 22, 1–16.

Liu, J., Li, E., Long, X., Zheng, M., Wang, J., Sang, H., 2004a. The metallogentic age of Dashankou gold deposit in Xinjiang, southwestern Tianshan Mountains. Journal of Jilin University (Earth Science Edition) 34 (1), 137–143 (in Chinese with English abstract).

Liu, J., He, M., Li, Z., Liu, Y., Li, C., 2004b. The oxygen and carbon isotopic geochemistry and its significance in Baiyangping silver-copper polymetallic metallogenic concentration area, Lanping Basin. Mineral Deposits 23, 1–10 (in Chinese with English abstract).

Long, X., Zheng, M., Zhang, S., Liu, J., 1998. Study on fluid inclusions of Sawaya'erdun gold deposit. Mineral Deposits 17, 973–976 (suppl., in Chinese).

Loshchinin, V.P., 1996. The problem of gold genesis at the Ordovician–Silurian deposits of Muruntau ore field (Western Uzbekistan). 30th International Geological Congress, Beijing, China, vol. 1/3, p. 780. Abstract.

Ludwig, K.R., 1996. ISOPLOT: a plotting and regression program for radiogenic-isotope data (Version 2.90). United States Geological Survey Open-File Report 91 (445), 1–47.

Lyon, G.L., Hulston, J.R., 1984. Carbon and hydrogen isotopic compositions of New Zealand geothermal gases. Geochimica et Cosmochimica Acta 48, 1161–1171.

Macdonald, G.A., Abbott, A.T., Peterson, F.L., 1983. Volcanoes in the Sea, the Geology of Hawaii, 2nd ed. University of Hawaii Press, Honolulu. 517 pp.

Mao, J., He, Y., Ding, T., 2002. Mantle fluids involved in metallogenesis of Jioadong (east Shandong) gold district: evidence of C, O and H isotopes. Mineral Deposits 21, 121–127 (in Chinese with English abstract).

Mao, J., Konopelko, D., Seltmann, R., Lehmann, B., Chen, W., Wang, Y., Eklund, O., Usubaliev, T., 2004. Postcollisional age of the Kumtor gold deposit and timing of Hercynian events in the Tien Shan, Kyrgyzstan. Economic Geology 99, 1771–1780.

Marakushev, A.A., Khokhlov, V.A., 1992. A petrological model for the genesis of the Muruntau gold deposit. International Geology Review 34, 59–76.

McCrea, J.M., 1950. The isotopic chemistry of carbonates and a paleotemperature scale. Journal of Chemical Physics 18, 849–857.

Mukhin, P.A., Savchuk, Y.S., Kolesnikov, A.V., 1988. The position of the "Muruntau lens" within the metamorphic rock unit of the Southern Tamdytau (Central Kyzylkum Desert). Geokhimiya 2, 64–72 (in Russian).

Ohmoto, H., 1972. Systematics of sulfur and carbon isotopes in hydrothermal ore deposits. Economic Geology 67, 551–578.

O'Neil, J.R., Silberman, M.L., 1974. Stable isotope relations in epithermal Au–Ag deposits. Economic Geology 69, 902–909.

Qin, Z., 1987. The mixing isochron model and its significance for isotopic chronology. Science in China. Series B, Chemistry, Life Sciences & Earth Sciences 30, 95–103.

Robin, M.B., Joaquin, R., Spencer, R.T., Richard, M.T., Joseph, L.W., 1999. Lead isotope compositions of Late Cretaceous and Early Tertiary igneous rocks and sulfide minerals in Arizona: implications for the sources of plutons and metals in porphyry copper deposits. Economic Geology 94, 211–244.

Rui, Z.Y., Goldfarb, R.J., Qiu, Y.M., Zhou, T.H., Chen, R.Y., Pirajno, F., Yun, G., 2002. Paleozoic — early Mesozoic gold deposits of the Xinjiang Autonomous Region, northwestern China. Mineralium Deposita 37, 393–418.

Sang, H., Wang, S., Hu, S., Qiu, Ji., 1994. $^{40}Ar/^{39}Ar$ dating method and Ar isotopic mass spectrometry analysis of quartz. Journal of Chinese Mass Spectrometry Society 15, 17–27 (in Chinese with English abstract).

Seltmann, R., Shatov, V., Yakubchuk A., eds., 2003. Mineral deposits database and thematic maps of Central Asia (scale 1:1,500,000), Explanatory Notes to GIS ArcView 3.2 and MapInfo v7 package: London, Centre for Russian and Central Asian Mineral Studies, Natural History Museum, 116 pp.

Shayakobov, T., Kremenetsky, A., Mintser, E., Obraztsov, A., Graupner, T., 1999. The Muruntau orefield. In: Islamov, F., Kremenetsky, A., Seltmann, R. (Eds.), Au, Ag, and Cu deposits of Uzbekistan. Excursion Guidebook of the IGCP-473 International Field Conference to Uzbekistan, 27 Aug. – 4 Sept. 1999. IAGOD Guidebook Series, vol. 7. GFZ, Potsdam, pp. 37–74.

Shelton, K.L., So, C.S., Haeussler, G.T., Chi, S.J., Lee, K.Y., 1990. Geochemical studies of the Tongyoung gold–silver deposits, Republic of Korea. Evidence of meteoric water dominance in a Te-bearing epithermal system. Economic Geology 85, 1114–1132.

Sheppard, S.M.F., 1986. Characterization and isotopic variations in natural waters. In: Valley, J.W., Taylor Jr., H.P., O'Neil, J.R. (Eds.), Stable Isotopes in High Temperature Geological Processes. Reviews in Mineralogy, vol. 16, pp. 165–183.

Skryabin, V.F., Guryanov, V.F., Dzhurayev, A.D., 1997. Primary geochemical zoning at Muruntau ore deposit. Razvedka i Okhrana Nedr (Exploration and Conservation of Resources) 11, 11–16 (in Russian).

Tan, G., 1983. A Concise Course in Paleontology. Geological Press, Beijing. 306 pp. (in Chinese).

Tan, K.R., 1993. Proceeding of superdeep drilling geology in Muruntau gold field. Gold Science & Technology 1, 17–28 (in Chinese with English abstract).

Tu, G., 2000. The Super-Large Ore Deposits in China. Science Press, Beijing, China. 266 pp.

Uspenskiy, Y.I., Aleshin, A.P., 1993. Patterns of scheelite mineralization in the Muruntau gold deposit, Uzbekistan. International Geology Review 35, 1037–1051.

Vollmer, R., 1976. Rb–Sr and U–Th–Pb systematics of alkaline rocks: the alkaline rocks from Italy. Geochimica et Cosmochimica Acta 40, 283–295.

Wang, S., Qiu, J., 1999. A study of saddle-shaped ^{40}Ar–^{39}Ar age spectrum of chert as exemplified by the Tieling Formation, Jixian section. Acta Geoscientia Sinica 20, 363–367 (in Chinese with English abstract).

Wang, Y., Yang, J., Tao, X., 1988. Experimental research on Sm–Nd isotopic method of fossil-mineral-rock and its application. Journal of Nanjing University (Science Edition) 20, 297–308 (in Chinese with English abstract).

Wang, C.Y., Zhou, M.K., Yan, Y.J., Wu, Y.L., Zhao, Y.G., Qian, Y.Z., 2000. Lower Devonian conodonts from the Sawaya'erdun gold mine area, Wuqia (Ulugqat) county, Xinjiang. Acta Micropalaeontologica Sinica 17, 255–264.

Wendt, I., Carl, C., 1991. The statistical distribution of the mean squared weighted deviation. Chemical Geology 86, 275–285.

Wilde, A.R., Layer, P., Mernagh, T., Foster, J., 2001. The giant Muruntau gold deposit: geologic, geochronlogic, and fluid inclusion constraints on ore genesis. Economic Geology 96, 633–644.

Wilkinson, J.J., Boyce, A.J., Earls, G., Fallick, A.E., 1999. Gold remobilization by low-temperature brines: evidence from the Curraghinalt gold deposit, Northern Ireland. Economic Geology 94, 289–296.

Wu, R., Tian, C., Huang, M., Cai, H., Zhi, Q., Qi, S., Cao, L., Wang, R., 1998. Geological characteristics of the gold–copper deposits in the western Tianshan. Journal of Precious Metallic Geology 7, 1–19 (in Chinese with English abstract).

Yakubchuk, A., Cole, A., Seltmann, R., Shatov, V., 2002. Tectonic setting, characteristics, and regional exploration criteria for gold mineralization in the Altaid orogenic collage: the Tien Shan province as a key example. Society of Economic Geologists Special Publication 9, 177–201.

Yang, F., Ye, Q., Fu, X., Ye, J., 1999. Distribution and metallogenic conditions of gold deposit in the southernwest Tianshan Mountains. Xinjiang Geology 17, 129–136 (in Chinese with English abstract).

Yang, J., Zhou, X., Chang, H., 2000. The Rb–Sr isochrology and metallogenic ages of Au-bearing minerals and ores in the Linlong gold deposit, Shandong. Chinese Science Bulletin 45, 1547–1553 (in Chinese).

Ye, J., Ye, Q., Meng, X., Wang, J., Zhang, X., 1998. The forming condition and prospecting of Muruntau type gold deposit in southwestern Tianshan, China. Mineral Deposits 17, 41–42 (suppl., in Chinese).

Ye, J., Wang, L., Ye, Q., Li, H., Zhang, X., 1999a. Metallogenic epoch and ore-bearing strata age of the Sawaya'erdun gold–antimony deposit in Tianshan Mountains, China. Acta Geoscientia Sinica 20, 278–283 (in Chinese with English abstract).

Ye, J., Ye, Q., Wang, J., Wu, Y., Yang, F., Fu, X., 1999b. Geochemistry and metallogenic mechanism of the Sawaya'erdun gold–antimony deposit. Mineral Deposits 18, 64–72 (in Chinese with English abstract).

Ye, Q., Ye, J., 1998. The mechanism and origin of Sawaya'erdun gold and antimony deposit in Xinjiang, China. Mineral Deposits 17, 287–290 (suppl., in Chinese).

Ying, H., 2002. ^{40}Ar–^{39}Ar fast neutron activation dating of gold-rich quartz vein from the Mojiang nickel-gold deposit, Yunnan. Chinese Journal of Geology 37, 107–109 (in Chinese with English abstract).

Ying, H., Liu, B., 2002. ^{40}Ar–^{39}Ar dating of gold-bearing quartz veins in the Fengyang and Zhangbaling areas, Anhui Province, and its geological significance. Mineral Deposits 21, 240–245 (in Chinese with English abstract).

York, D., 1969. Least squares fitting of a straight line with correlated errors. Earth and Planetary Science Letters 5, 320–324.

Yu, C.C., Lin, Y.D., Shi, Y., Huang, Z.X., Yu, X.G., 1983. Carboniferous and Permian Corals. Jilin People's Publishing House, Changchun. 357 pp. (in Chinese).

Zairi, N.M., Kurbanov, N.K., 1992. Isotopic-geochemical model of ore genesis in the Muruntau ore field. International Geology Review 34, 88–94.

Zartman, R.E., Doe, B.R., 1981. Plumbotectonics — the model. Tectonophysics 75, 135–162.

Zeitler, P.K., Gerald, D.F., 1986. Saddle-shaped $^{40}Ar/^{39}Ar$ age spectra from young, micro-structurally complex potassium feldspars. Geochimica et Cosmochimica Acta 50, 1185–1199.

Zhai, Y.S., 2006. Innovative research on mineral deposit geology. Earth Science Frontiers 13, 1–7.

Zhang, L., 1989. Petrogenetic and Mineragenetic Theories and Prospecting. Beijing University of Industry Press, Beijing. 200 pp. (in Chinese).

Zheng, Y., 1989. Influences of the nature of the initial Rb–Sr system on isochron. Chemical Geology. Isotope Geoscience Section 80, 1–16.

Zheng, M., Liu, J., Long, X., Tian, Z., 1996. Metallogenical Conditions and Prospects of Muruntau-Type Gold Deposits in the Southern Tianshan, Xinjiang. Chengdu University of Technology. 113 pp. (in Chinese).

Zheng, M., Liu, J., Long, X., Zhang, S., 1998. The first case of Muruntau-type gold deposit in China. Mineral Deposits 17, 381–384 (suppl., in Chinese with English abstract).

Zheng, M., Zhang, S., Liu, J., Long, X., Song, X., 2001. The Forming Setting of Muruntau-Type Gold Deposit in Southwestern Tianshan Mountains and Metallogenic Exploration. Geology Press, Beijing. 131 pp. (in Chinese).

Zheng, M., Liu, J., Zhang, S., Long, X., 2002. Isotopic composition and genetic indication of Sawaya'erdun gold deposit, Xinjiang. Journal of Chengdu University of Technology 29 (3), 237–245 (in Chinese with English abstract).

Zorikin, L.M., Starobinets, I.S., Stadnik, E.V., 1984. Natural Gas Geochemistry of Oil-Gas Bearing Basins. Mineral Press, Moscow, USSR. 164 pp. (in Russian).